

# Texture gradients and strain localisation in extruded aluminium profile

M. Khadyko<sup>1,\*</sup>, S. Dumoulin<sup>2</sup>, and O.S. Hopperstad<sup>1</sup>

<sup>1</sup> *Structural Impact Laboratory (SIMLab), Centre for Research-based Innovation, Department of Structural Engineering, Norwegian University of Science and Technology, NO-7491 Trondheim, Norway*

<sup>2</sup> *SINTEF Materials & Chemistry, NO-7465 Trondheim, Norway*

## Abstract

Through-thickness crystallographic texture gradients may develop in extruded profiles and rolled sheets of aluminium alloys. These texture gradients are often modelled using the crystal plasticity theory in order to predict strain localisation more accurately. In this work, an experimental and numerical study was carried out for a flat extruded profile with texture gradients made of the aluminium alloy AA6063. Uniaxial tension and plane-strain tension specimens were produced from this profile in two orthogonal material directions and heat treated to different tempers to study the role of crystallographic texture and work-hardening on strain localisation. The microstructure, including the orientation, morphology and position of the grains, was obtained from EBSD scans. The plane-strain tension tests were simulated using two crystal plasticity finite element models: the first represents accurately the measured microstructure, whereas the second one only represents correctly the global texture but not the texture gradients and grain morphology, i.e., the grain orientations are assigned randomly. In addition, a coarser model was used to identify the material parameters based on data from the plane-strain tension tests. The simulation results showed that accurate modelling of the microstructure did not improve the predictions significantly. The model with the same global texture but with random assignment of grain orientations gave similarly good predictions for both the global stress-strain behaviour and the local deformation patterns.

*Keywords: crystal plasticity; texture gradients; finite element method; plane-strain conditions; strain localisation.*

---

\* Corresponding author: Mikhail Khadyko (mikhail.khadyko@ntnu.no)

## 1. Introduction

The wide use of aluminium alloys in all sorts of industrial applications leads to an extensive research on the mechanical, chemical and physical properties of these materials and their connection to each other. Depending on the alloying elements and processing techniques, aluminium alloys have a broad range of microstructural features that define their macroscopic behaviour. This allows a certain degree of control over the properties of the produced material [1] but also requires complex material models and extensive experimental procedures to accurately describe these properties. Phenomenological material models consider the material as a homogeneous continuum, ignoring the microstructure but providing a convenient and computationally effective description of the material behaviour. This approach is especially important for engineering applications and is actively studied [2-4]. The real material is inhomogeneous at the microscale, consisting of a multitude of elastically and plastically anisotropic crystalline grains with different crystallographic orientations. Crystal plasticity (CP) models provide a more computationally heavy but also a more accurate description of the local mechanical fields by accounting for the physical mechanisms of plastic deformation by slip on specific crystallographic planes.

Flat profiles and sheets are produced by extrusion and rolling, respectively. For both of these types of products the thickness dimension is small compared to the other dimensions. The typical microstructures of flat extruded profiles and sheet metals also demonstrate many similarities. The properties of such products are extensively studied using among others crystal plasticity models. These models may be used to predict the macroscopic plastic anisotropy of the sheet if the crystallographic texture of the alloy is known [5, 6]. The behaviour of the material under various strain paths such as uniaxial and biaxial tension [7] and compression in rolling [8] may be described in more detail. Attempts have been made to use crystal plasticity models to predict forming limit diagrams of sheet metal, such as in [9-12]. Sheet metal and flat extruded profiles may be used for further production by deep drawing or pressing, or as a part of some structural components. In most cases, strain localisation, either by necking or shear banding, limits the ductility during manufacturing and application of the structural component. The small ratio between thickness and other dimensions means that the stress and strain fields may often be approximated using the plane-strain or plane-stress assumption. This simplifies the analytical and numerical description of strain localisation. The analytical solution of the localisation problem was first proposed by Hill in a seminal work [13] and further developed by Rice in [14], while a more recent

example of this approach may be found e.g. in [15]. The finite element method (FEM) is often used to model both local-necking and shear-banding type of problems. Some of the earliest works are [16, 17] and in [18-20] the same line of research is continued with more advanced material models, including the crystal plasticity models. These works showed that accurate prediction of strain localisation requires a detailed modelling of the crystallographic texture and its evolution during the deformation. Shear bands are initiated inside the grains and propagate through the grain boundaries, leading eventually to fracture [21], meanwhile the variation in grain strength, due to variation in orientation, creates the inhomogeneity that triggers the necking type instabilities.

The crystal plasticity theory is used widely to study these localisation phenomena. In [22-24], the strain localisation in thin-walled tubes under internal pressure is investigated. The localisation in deep drawing of monocrystalline copper is considered in [25], and in [26] banding in copper single crystals is used to validate an advanced crystal plasticity model. Ductile damage by void growth and fracture by void coalescence are tightly connected to the localisation processes, and attempts have been made to include damage mechanisms into the crystal plasticity models. Void growth in a single crystal cell is modelled in [27]. The void volume fraction is implemented directly into the hardening rule of a crystal plasticity model in [28]. The influence of particles on localisation and fracture in plane strain tension is modelled in [29], and an experimental and numerical study of localisation bands and damage in uniaxial tension is performed in [30]. Another phenomenon that cannot be predicted without considering the crystalline grains and texture is surface roughening [31-33].

The introduction of crystalline grains with different orientations and of crystallographic texture was a step towards a more accurate description of the polycrystalline structure of metals compared to the homogeneous continuum of the phenomenological models. The texture is a statistical concept, describing orientations of a large number of grains. Usually, for computational reasons, only a small part of a deforming body with a relatively small number of grains is modelled by crystal plasticity. The texture in this case is assumed to be the same for the whole body, invariant of the location where it is measured. But in many cases this is not true. The next step towards a more accurate material description would be to consider the variations of texture throughout the body and the influence of such variations on its mechanical properties.

Texture gradients often develop in sheets and flat extruded profiles during the production processes due to the boundary conditions on the outer layers. A finite element analysis of texture evolution during rolling and extrusion is used in [34-36] to investigate how this development proceeds. The experimental characterisation of texture gradients in rolled sheets and extruded flat profiles is found in [37, 38], and in [39, 40] methods for measuring and statistical modelling of the texture gradients are presented.

The influence of texture gradients on the plastic properties of metallic materials has become a topic of research in recent years as the available computational capabilities increased. The influence of texture gradients on shear banding in sheet metal is studied in [41] and [42]. Various loading cases are applied to materials with texture gradients in [43-46]. The relation between texture gradients and yield potentials of aluminium alloys is investigated in [47]. In some other cases, texture gradients may lead to spatial variation of the plastic flow anisotropy [48].

One way to model through-thickness texture gradients is to use crystal plasticity together with the finite element method (CP-FEM) and thus recreate the measured microstructure, including the morphology, position and orientation of the grains and eventually other features, such as the primary particles. If the number of grains is small and their size is large enough (e.g. aluminium or tantalum oligocrystals), the finite element mesh may represent these grains quite accurately. The simulation results may then be directly compared to the deformation fields obtained *in situ* with digital image correlation (DIC), such as in [49-53]. In other cases, the grains are too small or too numerous, and have to be modelled in a simplified manner, while keeping the general characteristic features of the microstructure intact [54, 55].

In this work, strain localisation under plane-strain tension was studied experimentally and numerically for flat extruded profiles made of the aluminium alloy AA6063. Uniaxial and plane-strain tension specimens were cut from an extruded profile in two orthogonal directions – along the extrusion direction (denoted the  $0^\circ$  orientation) and in the in-plane transverse direction (denoted the  $90^\circ$  orientation) of the profile. The specimens were then heat treated to different tempers and tested under quasi-static loading conditions in a universal testing machine. The applied force was measured by the load cell of the testing machine and DIC was used to measure the displacement fields and calculate the strain fields. The initial orientations of the crystalline grains were measured through the full thickness of the extruded profile with

electron backscatter diffraction (EBSD). These measurements were used to create an FE mesh that reproduces the spatial variation of the grain morphology through the thickness of the profile, the crystallographic texture and the misorientation distribution. In essence, the EBSD scan data was mapped onto the CP-FEM mesh. Another mesh was created for comparison, where the same number of grains and the same orientations were used, but where grain morphology, which was created using Voronoi tessellation, and grain orientations were assigned randomly. This mesh reproduces the measured crystallographic texture but neither the grain morphology nor the misorientation distribution. The experimental results of the plane-strain tension tests were used to calibrate the crystal plasticity model. CP-FEM with the two different meshes was used to simulate the plane-strain tension tests in two material directions with different work-hardening (which depends on the heat treatment). The simulation results were then compared with the experimental results in terms of global force-displacement curves and local deformation patterns at large strain. The deformed CP-FEM meshes were compared with microphotographs of the corresponding fractured test specimens. Both CP-FEM models gave reasonably good predictions of the force-displacement curves and demonstrated a combination of necking and shear banding as observed in the experiment. It was found that the orientation distribution through the thickness of the extruded profile has some effect on the initiation of shear banding, but ultimately the model with an accurate representation of the texture gradients did not demonstrate a clear superiority over the model with random orientation assignment in prediction of strain localisation.

## **2. Experiments**

DC-cast billets of the AA6063 alloy with a diameter of 203 mm were produced by Hydro Aluminium, Sunndal. The chemical composition of the alloy was (in weight %): 0.19 Fe, 0.44 Si, 0.45 Mg and Al balance. The material was homogenized in a batch homogenization furnace: it was heated at a rate of 200°C/h to 585°C, kept at 585°C for 5 hours, then cooled to room temperature at a rate larger than ~500°C/h. Billets were extruded to flat profiles with 205 mm width and 3 mm thickness using a billet temperature of 480°C, a container temperature of 440°C and a ram speed of 20 mm/s. All profiles were cooled with maximum spray cooling followed by forced air-cooling.

The uniaxial and plane-strain tension specimens were cut at 0° and 90° angles to the extrusion direction of the profile. The specimen geometries are presented in Figure 1. The specimens were subsequently heat treated to three different tempers. The details of the heat

treatments are given in Table 1. Three specimens of each type were produced for the two material directions and the three heat treatments, giving a total of 36 tests. The uniaxial and plane-strain tension tests were performed at average displacement rates of 0.5 mm/min and 0.3 mm/min, respectively, to ensure that the strain-rate effects were negligible. Prior to testing one of the specimen's surfaces was covered with a speckle pattern and this surface was photographed during testing with a Prosilica GC 2450 camera at 1 Hz frequency. The recorded images were analysed using the DIC method to obtain displacement and strain fields.

The FE DIC software Ecorr v2.0 [56] was used to measure the displacements and calculate the strains of the specimens. The DIC mesh was built from  $25 \times 25$  pixels elements, with an element size of approximately 0.7 mm, corresponding to a resolution of about 0.03 mm/pixel. The size of the images used for the analysis was  $2448 \times 2050$  pixels. The noise level estimated at the start of the test was not more than 0.05 pixels, or  $1.5 \cdot 10^{-4}$  mm for displacements and  $1.0 \cdot 10^{-3}$  for the strains. The DIC allows evaluating how closely the real strain field in the specimen approximated the ideal plane-strain condition. Figure 2 shows the field maps of the logarithmic normal strain components along two orthogonal directions in the plane of the specimen. The local strain in the central part of the specimen after localization along the width direction is less than 2%, while simultaneously the strain along the length direction is over 30%. In addition, the inhomogeneity of the strain field introduced by the notches is moderate in its extent, and thus the approximate plane-strain condition is fulfilled for a major part of the deforming zone of the specimen.

DIC was used to find the transverse strains in the uniaxial tension specimens. For convenience a coordinate system is introduced, with  $x$ -axis lying along the tension direction,  $y$ -axis along the width direction (in the profile plane) and  $z$ -axis in the thickness direction. The logarithmic strains were calculated for the DIC mesh elements placed approximately in the necking area. The logarithmic normal strains along the  $y$ - and  $z$ -axes are presented in Figure 3. The strain ratio  $r = d\varepsilon_y / d\varepsilon_z$  corresponds to the slope of the  $\varepsilon_y$  vs.  $\varepsilon_z$  curves in Figure 3. The strain ratio is fairly consistent for all three tempers, with  $r \approx 0.5$  for the  $0^\circ$  direction and  $r \approx 2$  (up to  $\varepsilon_y \approx -0.08$ ) for the  $90^\circ$  direction. Similar values were reported for the extruded AA6xxx alloys with strong cube textures [57].

The nominal stress-strain curves from the uniaxial tension tests are presented in Figure 4. The global displacements and strains were calculated between points of the DIC mesh that encompass the necking region but are initially in the homogeneously deforming part of the specimen. The initial distance between these points was around 60 mm. As expected, the heat treatment largely defines the yield strength and work-hardening of the material. The O temper has the lowest yield stress and the highest ductility, the T7 temper is the opposite, with the lowest ductility, and the T4 temper lies in-between these two extremes. The texture of the material leads to plastic anisotropy: while the yield strengths for the two orientations are very close, the difference in work-hardening is more significant and the stress level for the specimens in the  $0^\circ$  direction (or the extrusion direction) is in general higher than for the  $90^\circ$  direction. The force-displacement curves from the plane-strain tension tests are presented in Figure 5. The displacements were measured between points that encompass the deforming zone of the specimen, at a distance of 20 mm (marked with dots in Figure 1). The most notable trend is that the anisotropy of the two directions is reversed compared to uniaxial tension, with the forces in the  $90^\circ$  direction being significantly higher than those in the  $0^\circ$  direction. The influence of the heat treatment on the yield strength and work-hardening of the material is the same as in the case of uniaxial tension.

For comparison between the micromechanical models and the experiments, the average engineering stress-strain diagrams from the plane-strain tension tests were used. The average engineering stress was defined as the ratio of the total force to the initial cross-section area. The force was measured in the experiments for the whole specimen. In the simulation, the force corresponds to a part of the specimen in the central zone (with strict plane-strain conditions) having unit width. The force per unit width in the experiment is an average value that accounts for the broad central zone experiencing plane-strain conditions, but also the inhomogeneous stress and strain fields on the edges, see Figure 2. Yet, as already noticed, the error introduced by these zones should be moderate. The engineering strain was found from the edge-node displacement in the simulations and obtained by DIC in the experiments. A vector was defined on the DIC mesh, with length equal to the length of the CP-FEM model (6.7 mm, see Figure 1). The position of this vector was chosen in such a way that the final strain localisation initiated and developed in-between its ends. Thus, the two end points of this vector and the edge nodes of the CP-FEM models have a direct correspondence. The average engineering stress-strain diagrams for the tested specimens are shown in Figure 6.

The microstructure of the profile was studied with scanning electron microscopy. EBSD measurements were carried out in the plane defined by the extrusion direction (ED) and thickness (or normal) direction (ND) of the profile, using 5  $\mu\text{m}$  steps on a square grid. The grid size was  $3040 \times 2695 \mu\text{m}^2$  covering almost the whole thickness of the profile, except its outermost layers, thus providing 328860 measurement points. A total of 1147 grains with distinct orientations were identified in this area. The measurement results are presented in Figure 7. The grain orientation and morphology in different parts of the cross-section demonstrate some clear tendencies, with a central layer made of smaller grains ( $\leq 50 \mu\text{m}$ ) with approximately cube orientation, an intermediate layer with more or less randomly oriented large grains ( $\geq 100 \mu\text{m}$ ), and an outer layer composed of smaller grains with predominant Goss orientation. This orientation distribution is common for flat extruded Al profiles with recrystallized microstructure [44].

The orientation distribution function (ODF) presented in Figure 8, which represents the whole through-thickness texture, was calculated from pole figures in the EDAX TSL OIM software using a harmonic series expansion and triclinic sample symmetry [58]. Both the main cube and the minor Goss component may be identified in the ODF. The ODF was obtained from one of the specimens in T4 temper. The artificial heat treatments used to obtain tempers T7 and O should not induce any change of the grain structure and thus of the crystallographic texture. Nevertheless there are other mechanisms that may affect the plastic anisotropy of the T7 and O tempers, e.g. precipitate particles [59]. The plastic anisotropy of the tested materials may be evaluated using the data in Figure 3, Figure 4 and Figure 5. The plastic strain anisotropy presented in Figure 3 and the force-displacement curves for the plane-strain tension tests in Figure 5 show consistently similar behaviour for all three tempers. On the other hand, the stress-strain curves in Figure 4 show that for the O temper the stress anisotropy is considerably different from the one of the T4 and T7 tempers: the difference between the stress levels for the  $0^\circ$  and  $90^\circ$  orientations is much smaller. The anomalous flow stress in uniaxial tension for the  $0^\circ$  orientation that cannot be accounted for by the crystallographic texture influence alone has been described in the literature before [6, 57]. This effect diminishes with increasing strains, thus its effect on the localisation is expected to be insignificant, especially for the plane-strain tension tests. In addition, the consistency of the data in Figure 3 and Figure 5 indicates that the main source of the plastic anisotropy is the crystallographic texture and the crystal plasticity theory should adequately describe the evolution of the plastic deformation.

Another, less extensive EBSD scan was made in the plane defined by the thickness (or normal) direction (ND) and the in-plane transverse direction (TD). The results are presented in Figure 9. The grain morphology of the two normal planes is very similar, which justifies the use of the same EBSD scan data in the modelling of the tests in the 0° and 90° orientations.

### 3. Single crystal plasticity

The finite deformation framework is used in this work, where the total deformation gradient is multiplicatively decomposed into elastic and plastic parts [60]

$$\mathbf{F} = \mathbf{F}^e \mathbf{F}^p \quad (0)$$

The plastic part  $\mathbf{F}^p$  transforms the body from the initial undeformed configuration  $\Omega_0$  into the intermediate plastically deformed configuration  $\bar{\Omega}$  due to plastic slip, and the elastic part  $\mathbf{F}^e$  transforms the body from the intermediate into the current configuration  $\Omega$  with elastic deformation and rigid body rotation. The plastic velocity gradient  $\bar{\mathbf{L}}^p$  in the intermediate configuration is defined by

$$\bar{\mathbf{L}}^p = \dot{\mathbf{F}}^p (\mathbf{F}^p)^{-1} = \sum_{\alpha=1}^n \dot{\gamma}^\alpha \mathbf{m}_0^\alpha \otimes \mathbf{n}_0^\alpha \quad (0)$$

where the orthonormal vectors  $\mathbf{m}_0^\alpha$  and  $\mathbf{n}_0^\alpha$  are the slip direction and slip plane normal vectors, respectively, for slip system  $\alpha$  in the initial and intermediate configurations,  $\dot{\gamma}^\alpha$  is the slip rate on slip system  $\alpha$ , and  $n$  is the total number of slip systems.

The elastic Green strain tensor  $\bar{\mathbf{E}}^e$  with respect to the intermediate configuration is given by

$$\bar{\mathbf{E}}^e = \frac{1}{2}(\bar{\mathbf{C}}^e - \mathbf{I}), \quad \bar{\mathbf{C}}^e = (\mathbf{F}^e)^T \mathbf{F}^e \quad (0)$$

where  $\bar{\mathbf{C}}^e$  is the elastic right Cauchy-Green deformation tensor and  $\mathbf{I}$  is the unity tensor. The second Piola-Kirchhoff stress tensor  $\bar{\mathbf{S}}$  in the intermediate configuration reads as

$$\bar{\mathbf{S}} = \det \mathbf{F} (\mathbf{F}^e)^{-1} \boldsymbol{\sigma} (\mathbf{F}^e)^{-T} \quad (0)$$

where  $\boldsymbol{\sigma}$  is the Cauchy stress tensor. Since  $\bar{\mathbf{E}}^e$  and  $\bar{\mathbf{S}}$  constitute a power conjugate pair, a linear hyperelastic relation for small elastic strains is defined by

$$\bar{\mathbf{S}} = \bar{\mathbf{C}}_{el}^{\bar{\mathbf{S}}} : \bar{\mathbf{E}}^e \quad (0)$$

where  $\bar{\mathbf{C}}_{el}^{\bar{\mathbf{S}}}$  is the fourth order tensor of elastic moduli that has three independent components describing the elastic anisotropy of the crystal.

The plastic flow is described by a rate-dependent law

$$\dot{\gamma}^\alpha = \dot{\gamma}_0 \left( \frac{|\tau^\alpha|}{\tau_c^\alpha} \right)^{\frac{1}{m}} \text{sgn}(\tau^\alpha) \quad (0)$$

where  $\dot{\gamma}_0$  is the reference slip rate and  $m$  is the instantaneous strain rate sensitivity. The exponent  $m$  is here chosen to be sufficiently high ( $m = 200$ ) so that the plastic flow can be considered rate-insensitive, if not strictly rate-independent [61], and the strain rate should not affect the results. Further,  $\tau_c^\alpha$  is the yield strength of slip system  $\alpha$ , and the resolved shear stress  $\tau^\alpha$  is obtained as

$$\tau^\alpha = \bar{\mathbf{C}}^e \bar{\mathbf{S}} : (\mathbf{m}_0^\alpha \otimes \mathbf{n}_0^\alpha) \quad (0)$$

The hardening rate is defined by

$$\dot{\tau}_c^\alpha = \theta(\Gamma) \sum_{\beta=1}^n q_{\alpha\beta} |\dot{\gamma}^\beta| \quad (1)$$

where  $\theta(\Gamma)$  is the hardening modulus,  $q_{\alpha\beta}$  is the matrix of self-hardening and latent-hardening coefficients, and the accumulated slip  $\Gamma$  is defined by the evolution equation

$$\dot{\Gamma} = \sum_{\alpha=1}^n |\dot{\gamma}^\alpha| \quad (1)$$

The hardening modulus  $\theta(\Gamma)$  is defined as

$$\theta(\Gamma) = \sum_{k=1}^{N_f} \theta_k \exp\left(-\frac{\theta_k}{\tau_k} \Gamma\right) \quad (1)$$

where  $\theta_k$  and  $\tau_k$  are material parameters and  $N_V$  is the number of hardening terms. The initial slip resistance  $\tau_{c_0}^\alpha$  is assumed equal for all slip systems and is further denoted as  $\tau_0$ .

The single crystal model has been implemented as a user-material subroutine in the nonlinear finite element code LS-DYNA [62], using the explicit temporal integration scheme by Grujicic and Batchu [63]. The reader is referred to [64] for further details on the numerical implementation.

#### 4. Parameter identification

Some parameters of the crystal plasticity model, such as elastic constants, latent hardening coefficients and others, are assumed to be the same for all aluminium alloys and may be found in the literature. These parameters are presented in Table 2. AA6xxx alloys have been found to be rate-insensitive within a wide range of strain rates, e.g. [65], but not truly rate-independent. Therefore the parameters  $m$  and  $\dot{\gamma}_0$  for Al alloys are usually chosen in such a way that the viscoplastic relation in Equation (6) remains rate-insensitive, while its numerical implementation remains stable. For the rate-sensitivity, a frequently used value is  $m = 200$ . In [66] it is shown that for  $m = 200$ , the slip rates are practically the same as for the rate-independent case. Increasing the value led to overly stiff constitutive equations and prohibitively small time steps; decreasing it leads to introduction of rate-sensitivity and affects the localisation.

The unknown parameters are then the initial slip resistance  $\tau_0$  and the slip system hardening parameters  $\theta_k$  and  $\tau_k$  with  $N_V$  equal to 2 or 3 for the materials at hand. The standard method of finding these parameters by fitting the true stress-strain curve from a CP-FEM simulation to the experimental true stress-strain curve from a uniaxial tension test was considered. The main problem that arises in this case is obtaining the equivalent stress-strain curves after necking. Necking leads to inhomogeneous deformation and consequently inhomogeneous stress and strain fields, with a triaxial stress component caused by the neck constraint. For cylindrical specimens both numerical and analytical methods of extracting the equivalent stress-strain curve exist [67]. The flat rectangular cross-section shape complicates the task. Another problem is the CP-FEM modelling of the uniaxial tension test, which is necessary for the calibration of the crystal plasticity model. The inhomogeneous deformation after necking and the specimen cross-section geometry are both important factors that cannot

be neglected, but are very difficult to reproduce numerically, while keeping the CP-FEM model within reasonable size. Therefore it was chosen to use the results from the plane-strain tension tests for calibration. For plane-strain tension a two-dimensional FEM model may be used as a reasonable approximation, which allows studying the behaviour at large strains, including the localisation at lowered computational costs. The average engineering stress-strain curves from the CP-FEM model were fitted to the corresponding experimental curves by changing the hardening parameters.

The EBSD data was used as a basis for building all the FEM meshes. Because strain localisation was of primary interest, the size of the model should be large enough to allow both neck and shear bands to develop. To increase the size of the model and preserve the microstructure of the profile, the measured grain morphology was mirrored and the mirrored grains were assigned the same orientations as their original counterparts. The mesh used in the calibration procedure was constructed such that every  $10 \times 10$  points of the EBSD grid correspond to one finite element. Which grain this element belongs to, depends on which grain that constitutes the majority of the  $10 \times 10$  grid points. The element is then assigned the average orientation of the corresponding grain. As a result, a coarser, but generally similar, microstructure was reproduced, as shown in Figure 10. A total of 6588 elements was used. The smallest grains from the EBSD scan disappeared due to the large size of the interpolation cell. From the initial number of 1147 grains, the 899 largest grains were left. The model in Figure 10 contains 1726 grains (mirroring doubled all grains except 36 lying on the mirror axis). The length of the resulting model is 6.7 mm. The smallest grains are represented by just a few elements, while the largest ones consist of tens of elements. The colour coding in Figure 10 and all other relevant figures is the internal colour coding of LS-DYNA and does not correspond in any way to the orientations of the grains, unlike the EBSD scan data from Figure 7 and onwards, where the colours represent the crystallographic orientations. Nevertheless the orientations in the EBSD scan and the FEM models are practically identical.

The mesh is made of two-dimensional plane-strain elements with reduced integration (i.e., one integration point per element) and the Flanagan-Belytschko stiffness-based hourglass control [68]. The top and bottom edges of the model are free, corresponding to the free surfaces of the specimen. The nodes on the left extremity of the model are fixed in the tensile direction, while the velocity is smoothly ramped up to a constant value for the nodes on the right extremity. Boundary conditions to prevent rigid body motion were also prescribed.

The tests in the  $0^\circ$  direction were initially used in the calibration procedure, but a problem was encountered. The orientation distribution in the  $0^\circ$  direction turned out to have a group of softer grain orientations near the edge of the model, which deformed more easily and initiated a strain localisation near the constrained edge. This behaviour could lead to an additional error in the total force, so the tests in the  $90^\circ$  direction were used instead. In this case, the softer grains and the localisation area were situated close to the centre of the model, leading to a more realistic localisation process with the aforementioned boundary conditions.

To achieve loading in the  $90^\circ$  direction, the texture was rotated  $90^\circ$  around the appropriate axis. The explicit solver of the nonlinear FEM code LS-DYNA [62] was employed, using the crystal plasticity model to describe the material behaviour. Mass scaling was applied to reduce computation time and the kinetic energy was controlled at every step to ensure that it was very small compared to the total energy and that the simulation remained quasi-static.

To fit the stress-strain curve from the simulation to the experimental one, the optimization software LS-OPT was used [69]. LS-OPT ran several LS-DYNA simulations on every iteration with varied values of  $\tau_0$ ,  $\theta_k$  and  $\tau_k$ . It then compared the stress-strain curves from the simulations to the target experimental curve, calculated the mean squared error and changed the material parameters in such a way that in the next iteration the mean squared error was reduced. Usually 10-15 iterations of 8 simulations each were necessary for  $\tau_0$ ,  $\theta_k$  and  $\tau_k$  to converge to some value and for the mean squared error to reduce to a minimum. The obtained parameters are presented in Table 3.

Figure 11 shows the results of the fitting procedure. The model was able to achieve a very close fit to the experimental curves. For the T7 and T4 tempers, a two-term hardening rule was sufficient, while the two-term rule did not produce an equally good fit for the O temper and a three-term hardening rule was adopted.

## 5. Finite element modelling

The plane-strain tension tests were modelled using CP-FEM with material parameters obtained as described above. The mesh was constructed from the EBSD data in the way described in Section 4, except that a finer interpolation was used to obtain a more detailed model, i.e. every  $3 \times 3$  points of the EBSD grid now correspond to one finite element. The

resulting model is shown together with the mirrored EBSD scan in Figure 12. A total of 78480 elements were used, with 2258 grains corresponding to the EBSD scanned ones, i.e., all the 1147 grains from the scan are preserved and doubled by mirroring, except 36 grains on the mirror axis. The smallest grains are represented by just a few elements, while the largest ones consist of hundreds of elements. The other CP-FEM mesh in Figure 12 is created in Neper [70] by using Voronoi tessellation with random initial seed positions for the same 2258 grains as in the previous mesh. The same texture as the previous CP-FEM mesh was used but the orientations were assigned randomly to the grains. The grain shapes and positions are therefore not correlated with the real ones; only the general crystallographic texture is reproduced quite accurately. The numbers of nodes and elements are the same as in the previous mesh.

The FEM implementation is described in Section 4. The main difference between the FEM model used for the material calibration and the present simulation lies in the boundary conditions. To obtain more relaxed and realistic boundary conditions for the CP-FEM meshes, as well as to prevent early localisation too close to the edges of the mesh, additional elements were attached to both left and right edges of the polycrystal. The behaviour of these additional elements was described by  $J_2$  flow theory, including the von Mises yield function, the associated flow rule and nonlinear isotropic hardening. The evolution of the flow stress  $\kappa$  is described by a two-term Voce rule [71]

$$\kappa(\bar{\varepsilon}) = \kappa_0 + \sum_{i=1}^2 Q_i \left( 1 - \exp\left(-\frac{\theta_i}{Q_i} \bar{\varepsilon}\right) \right) \quad (2)$$

where  $\bar{\varepsilon}$  is the equivalent plastic strain,  $\kappa_0$  is the yield stress, and  $Q_i$  and  $\theta_i$  are the hardening parameters. The yield stress and hardening parameters for these additional elements were found by curve fitting to the true stress-strain curves obtained in the CP-FEM simulations with the calibration model, i.e., the  $J_2$  flow theory reproduces the average behaviour of the corresponding polycrystal. The parameters of the phenomenological plasticity model are given in Table 4. The nodes on the left extremity of the model are fixed in the tension direction, while a velocity is smoothly ramped up to a constant value for the nodes on the right extremity. Boundary conditions to prevent rigid body motion were also prescribed. The explicit solver of LS-DYNA was used as described in the previous section. The  $J_2$  flow theory is described by a standard LS-DYNA material model [62]. The simulations were run until the strains approximately corresponded to those at fracture in the experiments. All simulations

were run on one node of the Vilje supercomputer at the Norwegian University of Science and Technology [72], with the node consisting of two eight-core processors.

## 6. Results and discussion

To compare the response of the simulated plane-strain tension test with the experiment, the average engineering stress-strain diagrams were used. Figure 13, Figure 14 and Figure 15 show the results from the experiments, the simulations with the EBSD-mapped mesh and the simulations with the Voronoi tessellation mesh for tempers O, T4 and T7, respectively.

The CP-FEM models predicted the stress-strain curves before localisation reasonably well, considering the error introduced by the calibration procedure. The yielding point and the initial work-hardening rate were captured, as well as the plastic anisotropy stemming from the crystallographic texture. The two CP-FEM models, based on the EBSD scan and the Voronoi tessellation, respectively, produced virtually identical results. In the post-localisation stage, the predicted and experimental curves expectedly diverge more and the predictions from the two CP-FEM models start to diverge as well. Nevertheless, in most cases the CP-FEM models were quite successful in predicting both the initiation point of localisation and the force reduction rate. The error is the largest for the tests on tempers T4 and O in the  $0^\circ$  direction, where the force reduction rate was strongly underestimated by the CP-FEM models.

The primary source of error in the simulations is the calibration procedure. The CP-FEM model used is necessarily rather coarse. Even though the response of this model fits the experimental curve in the  $90^\circ$  direction very well, when the obtained material parameters were used in the finer model, a generally softer response with many individual variations was obtained. The principal problem is the following. On the one hand, to calibrate the material model in the large strain range, including the localisation regime, a refined FEM model is required to accurately describe the localisation process and the microstructure evolution. On the other hand, the fitting procedure consists of running multiple simulations of the material tests, which requires simplified FEM models with reasonable computation time.

In the previous simulations, the simulated response of the plane-strain tension specimen was obtained by a two-dimensional FEM model of the central part of the specimen. To test the validity of this modelling approach, the test specimen was modelled using 111830 8-node brick elements with reduced integration with the material described by the  $J_2$  flow theory. The mesh is presented in Figure 16. The boundary conditions of the test were

reproduced by fixing the faces of the specimen that were clamped in the test machine and applying constant velocity in the tension direction to the opposite pair of faces. The average engineering stress-strain curve was found for the three-dimensional model in the same way as for the test specimens. The parameters for temper T4 in the 90° direction were used in the simulation. The average engineering stress-strain curves from experiments and simulations with the original two-dimensional plane-strain model and the three-dimensional brick model (both using the  $J_2$  flow theory) are plotted in Figure 17. The difference in the response between the two- and three-dimensional models is not more than 5% for most of the strain range, except the very end of the deformation history, close to the fracture point. The results indicate that the original two-dimensional plane-strain model gives a reasonably accurate representation of the response of the plane-strain tension specimens. It may be argued that the correspondence between the two- and three-dimensional models may depend on the material model and be different for crystal plasticity, but testing this requires prohibitively large CP-FEM simulations.

One more aspect of the CP-FEM model that could affect the localisation description is the choice of element type. The use of brick elements vs. quadratic tetrahedral elements (or in the case of two-dimensional model, square elements vs. triangular elements) in the CP-FEM simulations is discussed in [73]. The brick elements have an intrinsic disadvantage that they cannot describe the grain boundary geometry precisely, producing a jagged surface, whereas the tetrahedral elements produce a more realistic smooth grain boundary. Nevertheless the global responses of the simulated polycrystal are equivalent for the models using the hexahedral and tetrahedral elements, provided that the mesh is sufficiently refined. On the other hand, [73] concludes that the local fields obtained with CP-FEM models using the brick elements should be used with caution, even though they are frequently used for localisation studies, see e.g. [18, 19].

After testing, a specimen of each temper-orientation combination was used to produce photographs of the microstructure within the failure area. The photographs were taken with an optical microscope in the centre of the specimens in a plane defined by the extrusion and thickness directions. The main characteristic feature of the deformed specimen is whether necking or shear banding is more pronounced at fracture. In Figure 18, Figure 19 and Figure 20, the photographs and the deformed meshes from the CP-FEM simulations are presented for the O, T4 and T7 temper, respectively. For the T4 and T7 tempers, the specimen with 0° orientation has a very developed neck at fracture, unlike the 90° specimen for which the shear

band defines the shape of the fracture surface. For the O temper, the photographs for both orientations show a similar well developed neck and less pronounced shear band influence. The simulations generally reproduced this trend for both CP-FEM models.

The shear bands emerge quite early in the deformation history, much earlier than the onset of necking. In Figure 21, the von Mises equivalent strain contours are shown for the T4 temper at 13 % global engineering strain in the  $0^\circ$  orientation, i.e., before necking occurs. The plastic strain field is already inhomogeneous at the intergranular level and some localised shear bands are already forming at the surface layer. The shear bands are even more pronounced in the T7 temper, as shown in Figure 21. Whether they will propagate and dominate the plastic deformation seems to depend mostly on the work-hardening of the material and the crystallographic texture and to much less extent on the spatial distribution of the grain orientations. The CP-FEM models based either on EBSD scan or on Voronoi tessellation give similar predictions for the same tempers and orientations. The delayed localisation in the case of the T4 and O temper in the  $0^\circ$  orientation led to the much lower force reduction rate than what is measured in the experiment. In this case the CP-FEM models gave similarly wrong predictions. The difference between the stress-strain curves produced by the two types of CP-FEM models is always quite small compared to the variation introduced by the work-hardening and the global crystallographic texture. This variation also has a random nature, and none of the two CP-FEM models gives consistently better predictions than the other.

To test the mesh sensitivity, an even finer CP-FEM model was created, where every element corresponds to one grid point of the EBSD scan, though the same average orientation is assumed for all elements constituting a grain. In Figure 22, the resulting von Mises equivalent strain is plotted for the T7 temper in the  $90^\circ$  orientation at around 10 % of global plastic strain and compared to a similar map from the baseline CP-FEM model described in Section 5. The shear bands in the model with higher mesh resolution are narrower and local plastic strain levels are somewhat higher, but the overall pattern of the shear banding is the same. The global response of the two models is also virtually the same.

## **7. Conclusion**

Uniaxial and plane-strain tension tests in two material directions were performed for a flat extruded profile made of the aluminium alloy AA6063 with three different heat treatments.

The extruded profile exhibited spatial variations of grain size and crystallographic texture over the thickness which is typically observed for such profiles. The plane-strain tension tests were modelled with CP-FEM, where these spatial variations in microstructure were accounted for. For comparison, a CP-FEM model with randomly generated microstructure but the same global texture was also used. The material parameters were calibrated using data from the plane-strain tension tests. In the pre-localisation regime, both CP-FEM models predicted the yield stress, the work-hardening rate and the plastic anisotropy observed in the experiments. In the post-localisation regime, the global behaviour was described by the stress-strain curves and the local behaviour by microphotographs of the fractured zone. The stress reduction in the engineering stress-strain curves was reproduced reasonably well with some notable exceptions. The local behaviour demonstrated a combination of necking and shear banding. The models predicted the main features of the observed local behaviour. The influence of the crystallographic texture gradient on the response proved to be small compared to the influence of the work-hardening and global texture. The exact reproduction of the texture gradients in the profile did not improve the predictions. On the other hand, a better identification of the work-hardening at large strains may considerably improve the accuracy of the localisation description.

## Acknowledgements

This research was supported in part with computational resources at NTNU provided by NOTUR, <http://www.notur.no>. The help of Trond Auestad in carrying out the experimental part of the work is appreciated. This work was partly financed by the Research Council of Norway through the project "Closing the gaps in multiscale materials modelling of precipitation free zones in alloys" (project no. 231762/F20) in the FRINATEK program.

## References

- [1] J. Hirsch and T. Al-Samman, "Superior light metals by texture engineering: optimized aluminum and magnesium alloys for automotive applications," *Acta Materialia*, vol. 61, pp. 818-843, 2013.
- [2] H. Aretz and F. Barlat, "New convex yield functions for orthotropic metal plasticity," *International Journal of Non-Linear Mechanics*, vol. 51, pp. 97-111, 2013.
- [3] F. Barlat, H. Aretz, J. Yoon, M. Karabin, J. Brem, and R. Dick, "Linear transformation-based anisotropic yield functions," *International Journal of Plasticity*, vol. 21, pp. 1009-1039, 2005.

- [4] F. Bron and J. Besson, "A yield function for anisotropic materials application to aluminum alloys," *International Journal of Plasticity*, vol. 20, pp. 937-963, 2004.
- [5] Y. An, H. Vegter, L. Carless, and M. Lambriks, "A novel yield locus description by combining the Taylor and the relaxed Taylor theory for sheet steels," *International Journal of Plasticity*, vol. 27, pp. 1758-1780, 2011.
- [6] S. Dumoulin, O. Engler, O. Hopperstad, and O. Lademo, "Description of plastic anisotropy in AA6063-T6 using the crystal plasticity finite element method," *Modelling and Simulation in Materials Science and Engineering*, vol. 20, p. 055008, 2012.
- [7] M. Iadicola, L. Hu, A. Rollett, and T. Foecke, "Crystal plasticity analysis of constitutive behavior of 5754 aluminum sheet deformed along bi-linear strain paths," *International Journal of Solids and Structures*, vol. 49, pp. 3507-3516, 2012.
- [8] G. Deng, A. K. Tieu, L. Si, L. Su, C. Lu, H. Wang, M. Liu, H. Zhu, and X. Liu, "Influence of cold rolling reduction on the deformation behaviour and crystallographic orientation development," *Computational Materials Science*, vol. 81, pp. 2-9, 2014.
- [9] R. Chiba, H. Takeuchi, M. Kuroda, T. Hakoyama, and T. Kuwabara, "Theoretical and experimental study of forming-limit strain of half-hard AA1100 aluminium alloy sheet," *Computational Materials Science*, vol. 77, pp. 61-71, 2013.
- [10] M. Mohammadi, A. P. Brahme, R. K. Mishra, and K. Inal, "Effects of post-necking hardening behavior and equivalent stress-strain curves on the accuracy of M-K based forming limit diagrams," *Computational Materials Science*, vol. 85, pp. 316-323, 2014.
- [11] Y. Tadano, N. Kuwashiro, and S. Hagihara, "Effect of Texture on Plastic Flow Localization of FCC Polycrystals Using Homogenization-Based Polycrystalline Plasticity," in *Key Engineering Materials*, 2015, pp. 450-455.
- [12] M. Hajian and A. Assempour, "Experimental and numerical determination of forming limit diagram for 1010 steel sheet: a crystal plasticity approach," *The International Journal of Advanced Manufacturing Technology*, pp. 1-11, 2014.
- [13] R. Hill, "On discontinuous plastic states, with special reference to localized necking in thin sheets," *Journal of the Mechanics and Physics of Solids*, vol. 1, pp. 19-30, 1952.
- [14] J. R. Rice, "The localization of plastic deformation," in *Proceedings of the 14th International Congress on Theoretical and Applied Mechanics*, Delft, 1976, pp. 207-220.
- [15] G. Franz, F. Abed-Meraim, and M. Berveiller, "Strain localization analysis for single crystals and polycrystals: Towards microstructure-ductility linkage," *International Journal of Plasticity*, vol. 48, pp. 1-33, 2013.
- [16] V. Tvergaard, A. Needleman, and K. K. Lo, "Flow localization in the plane strain tensile test," *Journal of the Mechanics and Physics of Solids*, vol. 29, pp. 115-142, 1981.
- [17] J. W. Hutchinson and V. Tvergaard, "Shear band formation in plane strain," *International Journal of Solids and Structures*, vol. 17, pp. 451-470, 1981.
- [18] M. Kuroda and V. Tvergaard, "Effects of texture on shear band formation in plane strain tension/compression and bending," *International Journal of Plasticity*, vol. 23, pp. 244-272, 2007.
- [19] K. Inal, P. Wu, and K. Neale, "Instability and localized deformation in polycrystalline solids under plane-strain tension," *International Journal of Solids and Structures*, vol. 39, pp. 983-1002, 2002.
- [20] L. Anand and S. Kalidindi, "The process of shear band formation in plane strain compression of fcc metals: effects of crystallographic texture," *Mechanics of Materials*, vol. 17, pp. 223-243, 1994.

- [21] L. Mattei, D. Daniel, G. Guiglionda, H. Klöcker, and J. Driver, "Strain localization and damage mechanisms during bending of AA6016 sheet," *Materials Science and Engineering: A*, vol. 559, pp. 812-821, 2013.
- [22] Y. Shi, P. Wu, D. Lloyd, and J. Embury, "Crystal plasticity based analysis of localized necking in aluminum tube under internal pressure," *European Journal of Mechanics-A/Solids*, vol. 29, pp. 475-483, 2010.
- [23] W. Zhuang, S. Wang, J. Cao, J. Lin, and C. Hartl, "Modelling of localised thinning features in the hydroforming of micro-tubes using the crystal-plasticity FE method," *The International Journal of Advanced Manufacturing Technology*, vol. 47, pp. 859-865, 2010.
- [24] W. Zhuang, S. Wang, J. Lin, D. Balint, and C. Hartl, "Experimental and numerical investigation of localized thinning in hydroforming of micro-tubes," *European Journal of Mechanics-A/Solids*, vol. 31, pp. 67-76, 2012.
- [25] X. Geng, B. Wang, Y. Zhang, J. Huang, M. Duan, and K. Zhang, "Effect of crystalline anisotropy and forming conditions on thinning and rupturing in deep drawing of copper single crystal," *Journal of Materials Processing Technology*, vol. 213, pp. 574-580, 2013.
- [26] M. A. Kumar and S. Mahesh, "Banding in single crystals during plastic deformation," *International Journal of Plasticity*, vol. 36, pp. 15-33, 2012.
- [27] S. Yerra, C. Tekog, F. Scheyvaerts, L. Delannay, P. Van Houtte, and T. Pardoen, "Void growth and coalescence in single crystals," *International Journal of Solids and Structures*, vol. 47, pp. 1016-1029, 2010.
- [28] G. Rousselier and M. Luo, "A fully coupled void damage and Mohr–Coulomb based ductile fracture model in the framework of a Reduced Texture Methodology," *International Journal of Plasticity*, vol. 55, pp. 1-24, 2014.
- [29] X. Hu, D. S. Wilkinson, M. Jain, and R. K. Mishra, "A parametric finite element study and an analytical model of particle distributions on post-necking deformation and failure mode in AA5754 aluminum alloy sheets," *International Journal of Fracture*, vol. 164, pp. 167-183, 2010.
- [30] C. Labergere, B. Guelorget, and M. Francois, "Strain rate distribution and localization band width evolution during tensile test," *International Journal of Solids and Structures*, vol. 51, pp. 3944-3961, 2014.
- [31] H. Li, Z. Jiang, and D. Wei, "Crystal plasticity finite modelling of 3D surface asperity flattening in uniaxial planar compression," *Tribology Letters*, vol. 46, pp. 101-112, 2012.
- [32] Z. Jiang, D. Wei, and H. Li, "Finite element modelling of surface roughness transfer and oxide scale micro deformation in metal manufacturing process," *AIP Conference Proceedings*, vol. 1532, pp. 254-261, 2013.
- [33] P. Groche, R. Schäfer, H. Justinger, and M. Ludwig, "On the correlation between crystallographic grain size and surface evolution in metal forming processes," *International Journal of Mechanical Sciences*, vol. 52, pp. 523-530, 2010.
- [34] K.-H. Jung, D.-K. Kim, Y.-T. Im, and Y.-S. Lee, "Crystal Plasticity Finite Element Analysis of Texture Evolution during Rolling of fcc Polycrystalline Metal," *Materials Transactions*, vol. 54, pp. 769-775, 2013.
- [35] K.-H. Jung, D.-K. Kim, Y.-T. Im, and Y.-S. Lee, "Prediction of the effects of hardening and texture heterogeneities by finite element analysis based on the Taylor model," *International Journal of Plasticity*, vol. 42, pp. 120-140, 2013.
- [36] F. Perocheau and J. Driver, "Texture gradient simulations for extrusion and reversible rolling of FCC metals," *International Journal of Plasticity*, vol. 16, pp. 73-89, 2000.

- [37] X. Zeng, M. Ahmad, and O. Engler, "Texture gradient, average texture, and plastic anisotropy in various Al–Li sheet alloys," *Materials Science and Technology*, vol. 10, pp. 581-591, 1994.
- [38] M. Chen, J. Li, Y. Zhao, H. Yuan, and W. Liu, "Comparison of texture evolution between different thickness layers in cold rolled Al–Mg alloy," *Materials Characterization*, vol. 62, pp. 1188-1195, 2011.
- [39] S. Li, F. Sun, and H. Li, "Observation and modeling of the through-thickness texture gradient in commercial-purity aluminum sheets processed by accumulative roll-bonding," *Acta Materialia*, vol. 58, pp. 1317-1331, 2010.
- [40] M. Miller and T. Turner, "A methodology for measuring and modeling crystallographic texture gradients in processed alloys," *International Journal of Plasticity*, vol. 17, pp. 783-805, 2001.
- [41] K. Neale, K. Inal, and P. Wu, "Effects of texture gradients and strain paths on localization phenomena in polycrystals," *International Journal of Mechanical Sciences*, vol. 45, pp. 1671-1686, 2003.
- [42] X. Hu, G. A. Cingara, D. S. Wilkinson, M. Jain, P. Wu, and R. K. Mishra, "Studies of Texture Gradients in the Localized Necking Band of AA 5754 by EBSD and Microstructure-Based Finite Element Modeling," *Computers, Materials, & Continua*, vol. 14, pp. 99-124, 2010.
- [43] I. Tikhovskiy, D. Raabe, and F. Roters, "Simulation of the deformation texture of a 17% Cr ferritic stainless steel using the texture component crystal plasticity finite element method considering texture gradients," *Scripta Materialia*, vol. 54, pp. 1537-1542, 2006.
- [44] M. Luo and G. Rousselier, "Modeling of large strain multi-axial deformation of anisotropic metal sheets with strength-differential effect using a Reduced Texture Methodology," *International Journal of Plasticity*, vol. 53, pp. 66-89, 2014.
- [45] J. Gawad, D. Banabic, A. Van Bael, D. S. Comsa, M. Gologanu, P. Eyckens, P. Van Houtte, and D. Roose, "An evolving plane stress yield criterion based on crystal plasticity virtual experiments," *International Journal of Plasticity*, 2015.
- [46] M. Dunand, A. P. Maertens, M. Luo, and D. Mohr, "Experiments and modeling of anisotropic aluminum extrusions under multi-axial loading–Part I: Plasticity," *International Journal of Plasticity*, vol. 36, pp. 34-49, 2012.
- [47] X.-H. Zeng and F. Barlat, "Effects of texture gradients on yield loci and forming limit diagrams in various aluminum-lithium sheet alloys," *Metallurgical and Materials Transactions A*, vol. 25, pp. 2783-2795, 1994.
- [48] M. Ghosh, A. Miroux, and L. Kestens, "Correlating r-value and through thickness texture in Al–Mg–Si alloy sheets," *Journal of Alloys and Compounds*, vol. 619, pp. 585-591, 2015.
- [49] G. Zhu, X. Hu, J. Kang, R. K. Mishra, and D. S. Wilkinson, "Deformation inhomogeneity in large-grained AA5754 sheets," *Materials Science and Engineering: A*, vol. 528, pp. 4187-4198, 2011.
- [50] A. Saai, H. Louche, L. Tabourot, and H. Chang, "Experimental and numerical study of the thermo-mechanical behavior of Al bi-crystal in tension using full field measurements and micromechanical modeling," *Mechanics of Materials*, vol. 42, pp. 275-292, 2010.
- [51] H. Lim, J. Carroll, C. Battaile, T. Buchheit, B. Boyce, and C. Weinberger, "Grain-scale experimental validation of crystal plasticity finite element simulations of tantalum oligocrystals," *International Journal of Plasticity*, vol. 60, pp. 1-18, 2014.
- [52] C. Badulescu, M. Grédiac, H. Haddadi, J.-D. Mathias, X. Balandraud, and H.-S. Tran, "Applying the grid method and infrared thermography to investigate plastic

- deformation in aluminium multicrystal," *Mechanics of Materials*, vol. 43, pp. 36-53, 2011.
- [53] X. Hu, D. Wilkinson, M. Jain, P. Wu, and R. Mishra, "The impact of particle distributions and grain-level inhomogeneities on post-necking deformation and fracture in AA5754 sheet alloys during uniaxial tension," *Materials Science and Engineering: A*, vol. 528, pp. 2002-2016, 2011.
- [54] A. Saai, I. Westermann, S. Dumoulin, and O. Hopperstad, "Crystal plasticity finite element simulations of pure bending of aluminium alloy AA7108," *International Journal of Material Forming*, pp. 1-13, 2015.
- [55] K. Inal, R. K. Mishra, and O. Cazacu, "Forming simulation of aluminum sheets using an anisotropic yield function coupled with crystal plasticity theory," *International Journal of Solids and Structures*, vol. 47, pp. 2223-2233, 2010.
- [56] E. Fagerholt, "Field measurements in mechanical testing using close-range photogrammetry and digital image analysis," 2012.
- [57] M. Khadyko, S. Dumoulin, G. Cailletaud, and O. Hopperstad, "Latent hardening and plastic anisotropy evolution in AA6060 aluminium alloy," *International Journal of Plasticity*, vol. 76, pp. 51-74, 2016.
- [58] O. Engler and V. Randle, *Introduction to texture analysis: macrotexture, microtexture, and orientation mapping*: CRC press, 2010.
- [59] N. Anjabin, A. Karimi Taheri, and H. Kim, "Crystal plasticity modeling of the effect of precipitate states on the work hardening and plastic anisotropy in an Al–Mg–Si alloy," *Computational Materials Science*, vol. 83, pp. 78-85, 2014.
- [60] E. Lee and D. Liu, "Finite-Strain Elastic—Plastic Theory with Application to Plane-Wave Analysis," *Journal of Applied Physics*, vol. 38, pp. 19-27, 1967.
- [61] J. Pan and J. R. Rice, "Rate sensitivity of plastic flow and implications for yield-surface vertices," *International Journal of Solids and Structures*, vol. 19, pp. 973-987, 1983.
- [62] J. O. Hallquist, "LS-DYNA theory manual," *Livermore software technology corporation*, vol. 3, 2006.
- [63] M. Grujicic and S. Batchu, "Crystal plasticity analysis of earing in deep-drawn OFHC copper cups," *Journal of Materials Science*, vol. 37, pp. 753-764, 2002.
- [64] S. Dumoulin, O. Hopperstad, and T. Berstad, "Investigation of integration algorithms for rate-dependent crystal plasticity using explicit finite element codes," *Computational Materials Science*, vol. 46, pp. 785-799, 2009.
- [65] Y. Chen, A. Clausen, O. Hopperstad, and M. Langseth, "Stress–strain behaviour of aluminium alloys at a wide range of strain rates," *International Journal of Solids and Structures*, vol. 46, pp. 3825-3835, 2009.
- [66] T. Mánik and B. Holmedal, "Review of the Taylor ambiguity and the relationship between rate-independent and rate-dependent full-constraints Taylor models," *International Journal of Plasticity*, vol. 55, pp. 152-181, 2014.
- [67] M. Khadyko, S. Dumoulin, T. Børvik, and O. Hopperstad, "An experimental-numerical method to determine the work-hardening of anisotropic ductile materials at large strains," *International Journal of Mechanical Sciences*, vol. 88, pp. 25-36, 2014.
- [68] D. Flanagan and T. Belytschko, "A uniform strain hexahedron and quadrilateral with orthogonal hourglass control," *International Journal for Numerical Methods in Engineering*, vol. 17, pp. 679-706, 1981.
- [69] N. Stander, W. Roux, T. Goel, T. Eggleston, and K. Craig, "LS-OPT user's manual," *Livermore software technology corporation*, 2008.

- [70] R. Quey, P. Dawson, and F. Barbe, "Large-scale 3D random polycrystals for the finite element method: Generation, meshing and remeshing," *Computer Methods in Applied Mechanics and Engineering*, vol. 200, pp. 1729-1745, 2011.
- [71] E. Voce, "The relationship between stress and strain for homogeneous deformation," *Journal of the Institute of Metals*, vol. 74, pp. 537-562, 1948.
- [72] <https://www.hpc.ntnu.no/display/hpc/Vilje>.
- [73] O. Diard, S. Leclercq, G. Rousselier, and G. Cailletaud, "Evaluation of finite element based analysis of 3D multicrystalline aggregates plasticity: Application to crystal plasticity model identification and the study of stress and strain fields near grain boundaries," *International Journal of Plasticity*, vol. 21, pp. 691-722, 2005.

## Figures

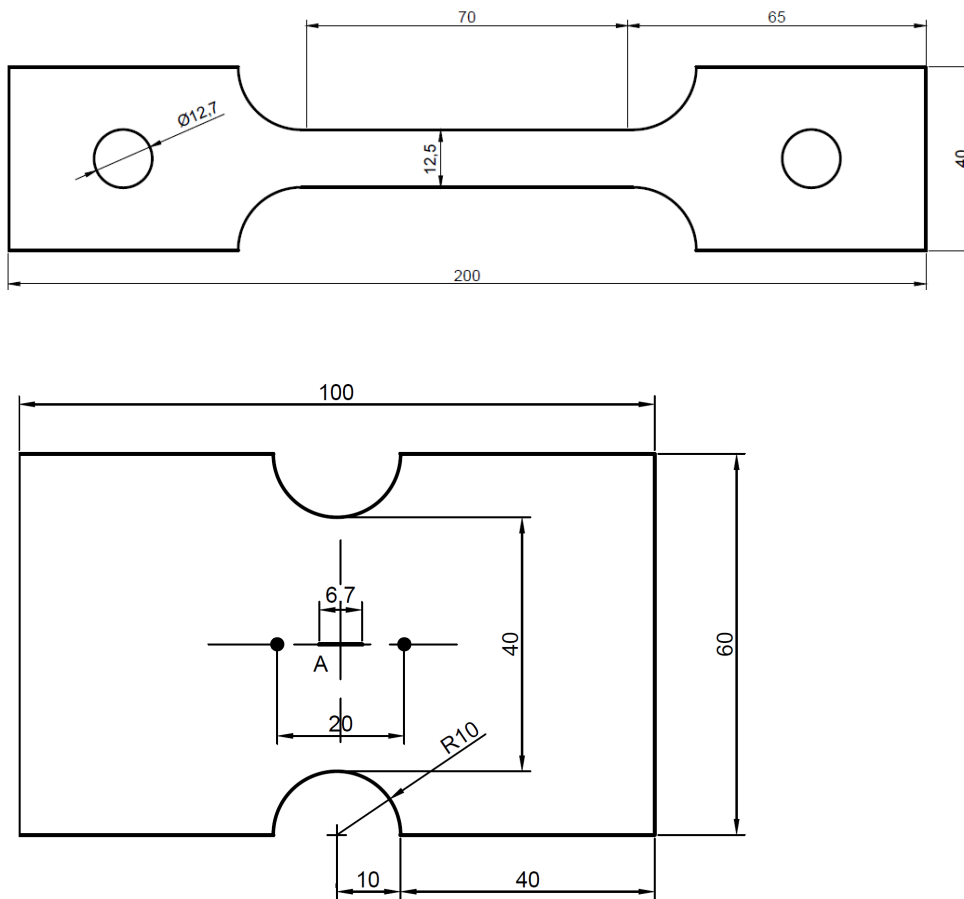


Figure 1: Test sample geometry for uniaxial tension (top) and plane-strain tension (bottom). The letter A denotes the through-thickness part of the gauge region that was modelled with CP-FEM by assuming plane-strain conditions.

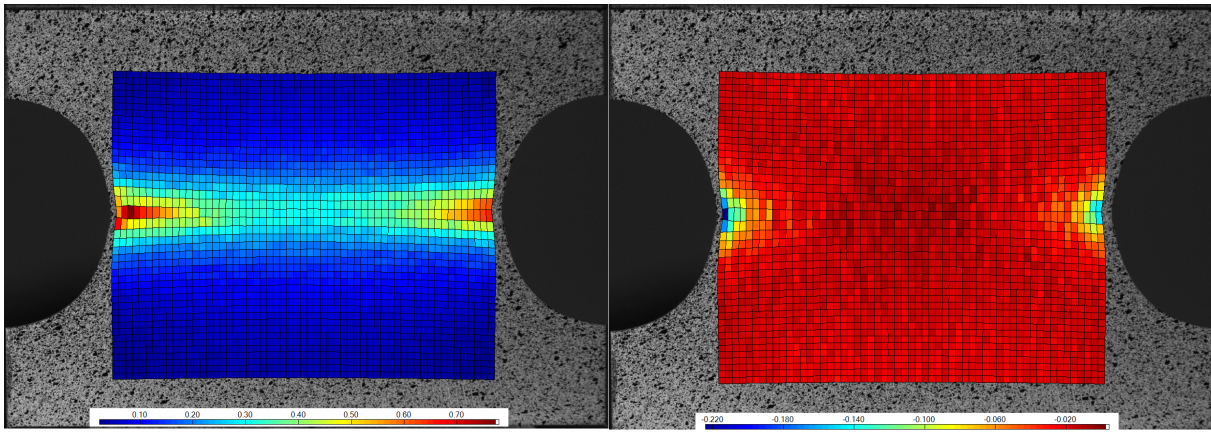


Figure 2: Field map of the logarithmic normal strain along length (left) and width (right) direction obtained with DIC from the plane-strain tension test of temper T4 in the  $0^\circ$  orientation.

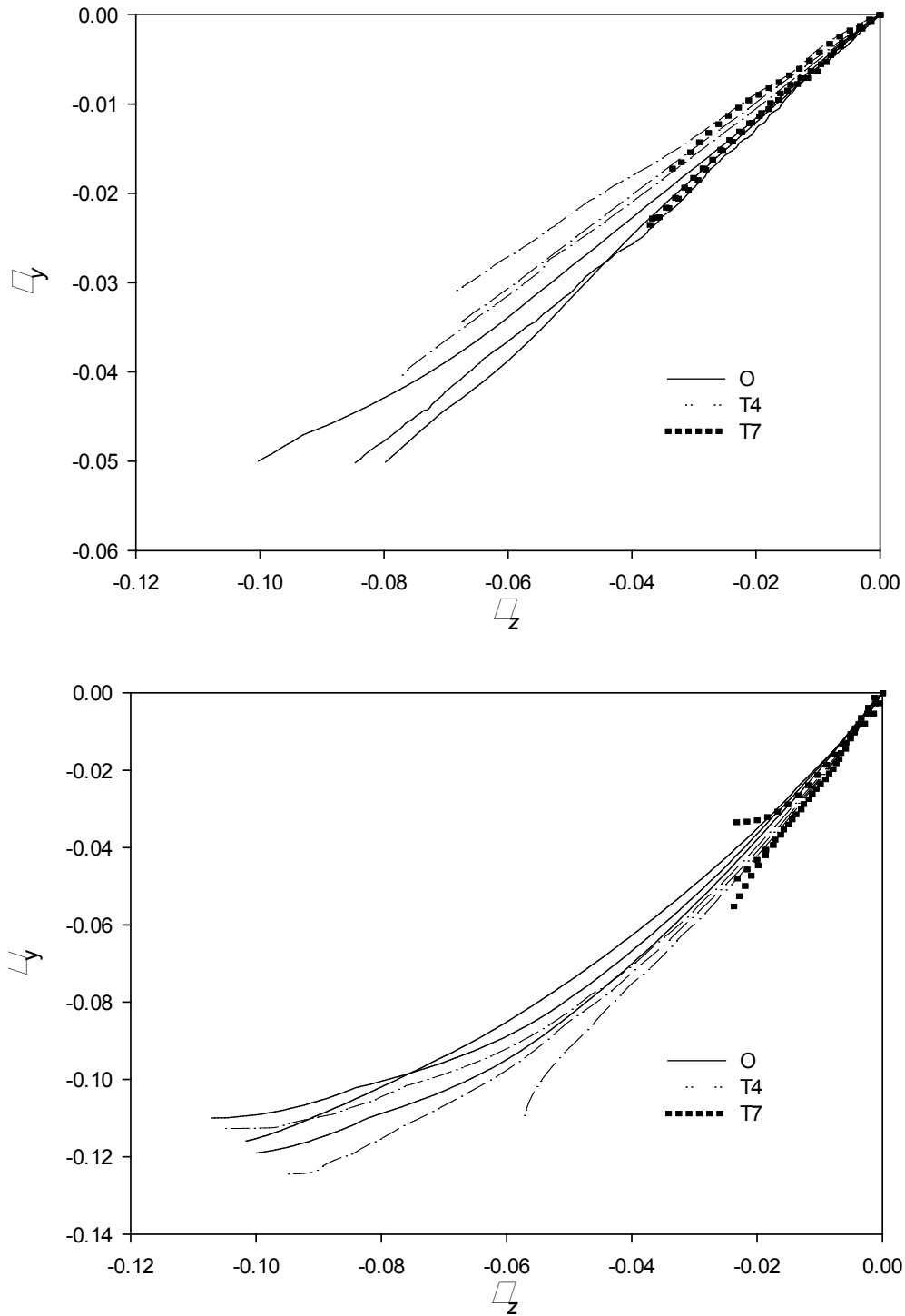


Figure 3: Logarithmic strains in thickness direction ( $\varepsilon_z$ ) vs. width direction ( $\varepsilon_y$ ) in the uniaxial tension specimen, measured in an element of the DIC mesh in the necking area for the  $0^\circ$  orientation (top) and  $90^\circ$  orientation (bottom).

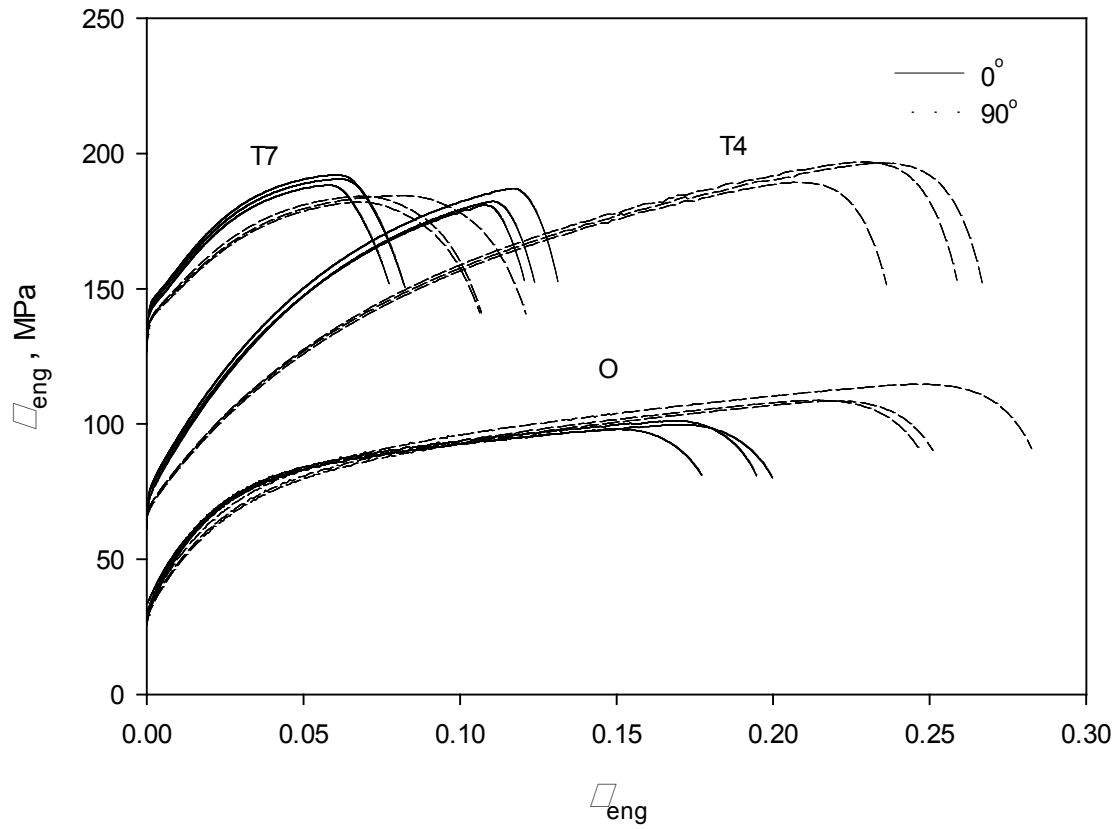


Figure 4: Engineering stress-strain curves from uniaxial tension tests in two material directions for three heat treatments of the AA6063 alloy.

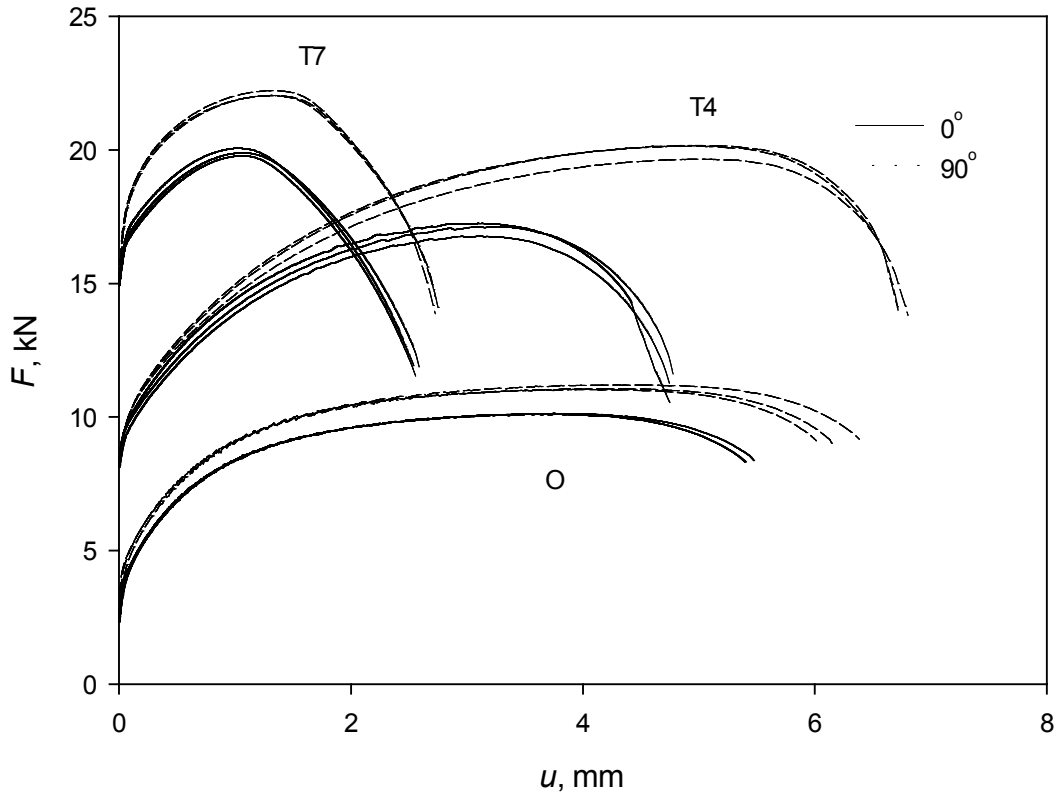


Figure 5: Force vs. displacement curves from the plane-strain tension tests in two material directions for three heat treatments of the AA6063 alloy.

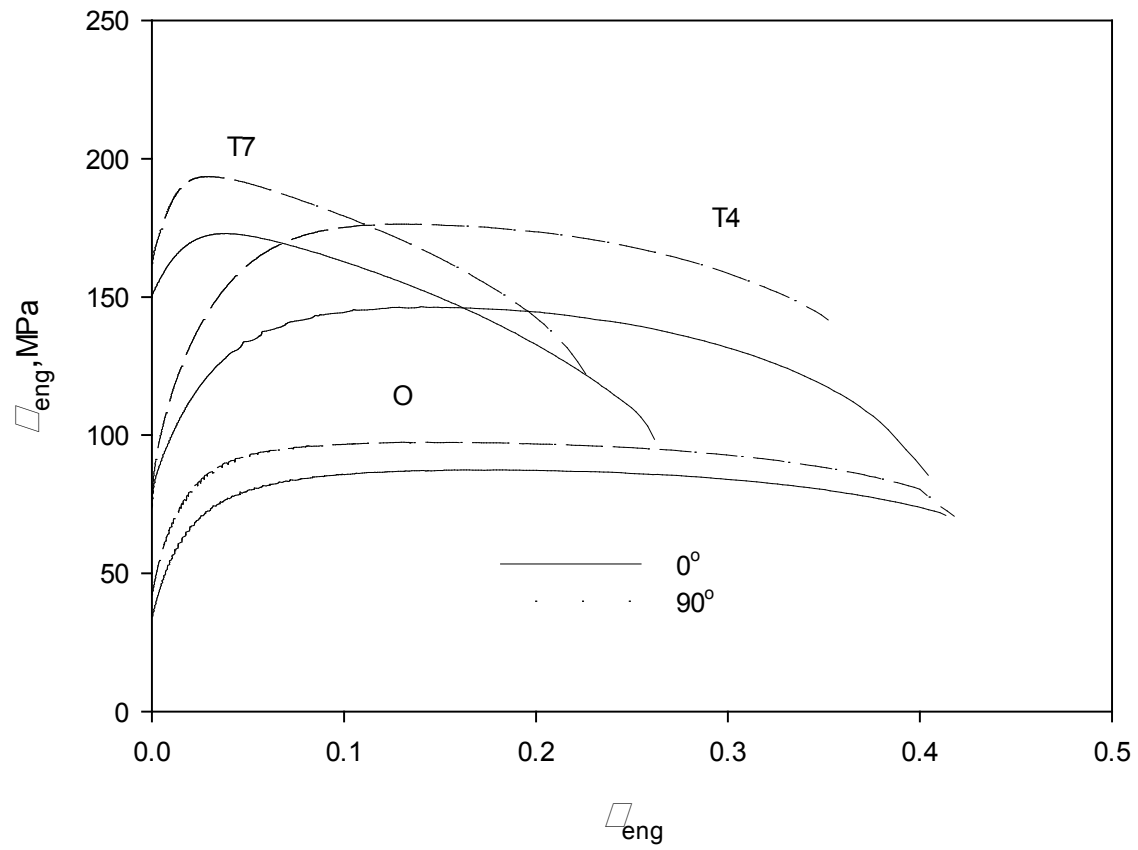


Figure 6: Engineering stress-strain curves in plane-strain tension from experiments, where the strains are calculated in the central part of the specimen (gauge length equal to 6.7 mm).

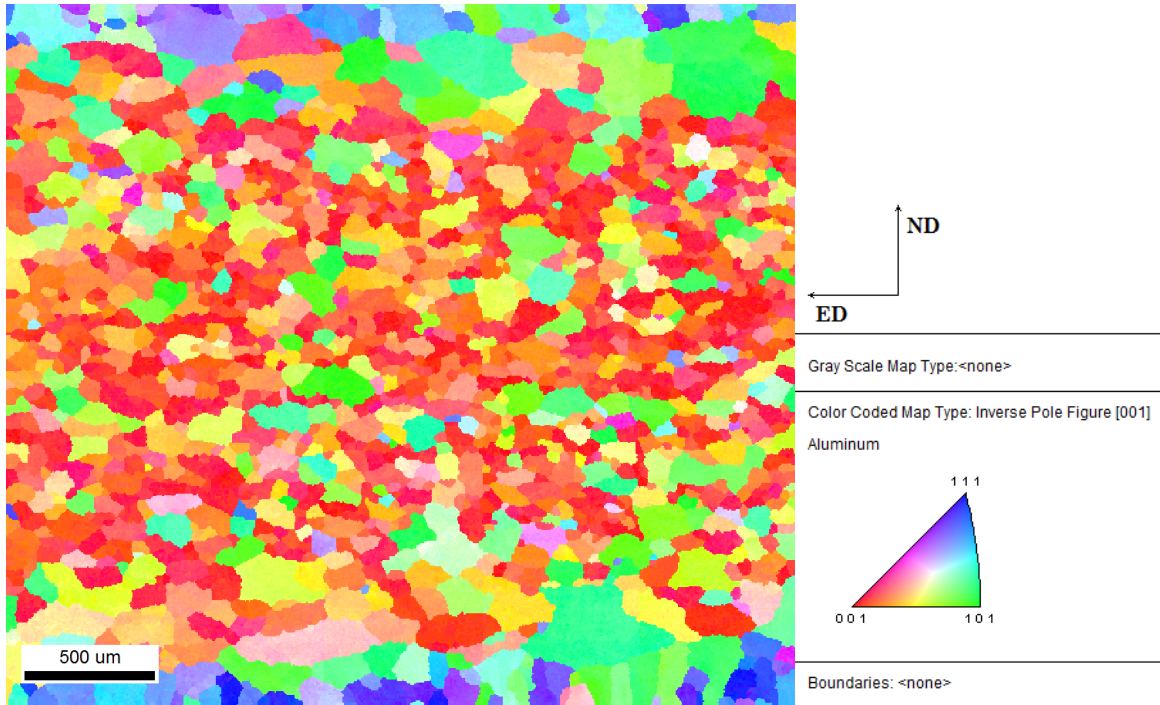


Figure 7: Electron backscatter diffraction (EBSD) scan showing the morphology, size and orientation of the grains through the thickness of the extruded AA6063 profile.

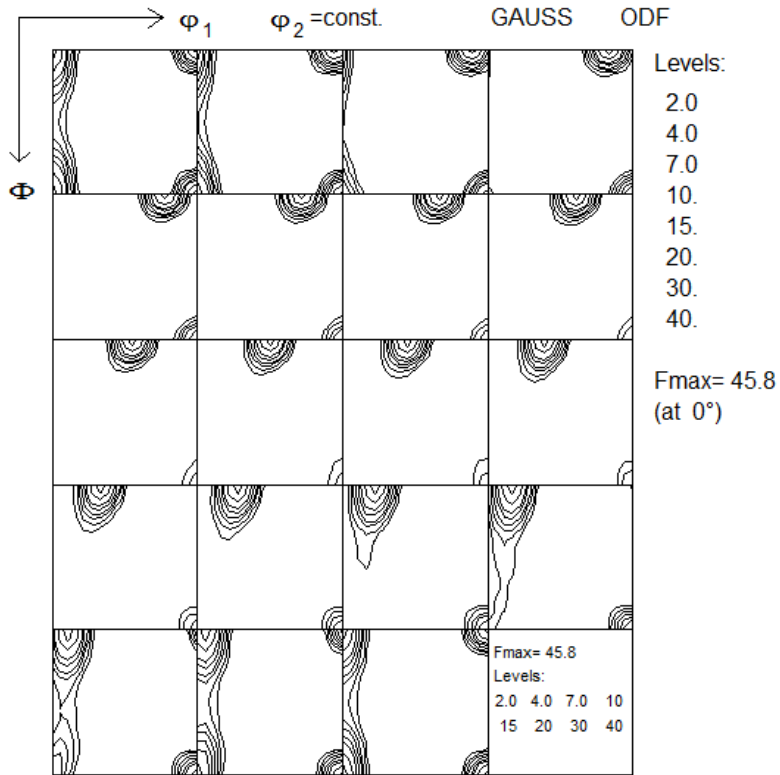


Figure 8: Orientation distribution function (ODF) for the AA6063 alloy.

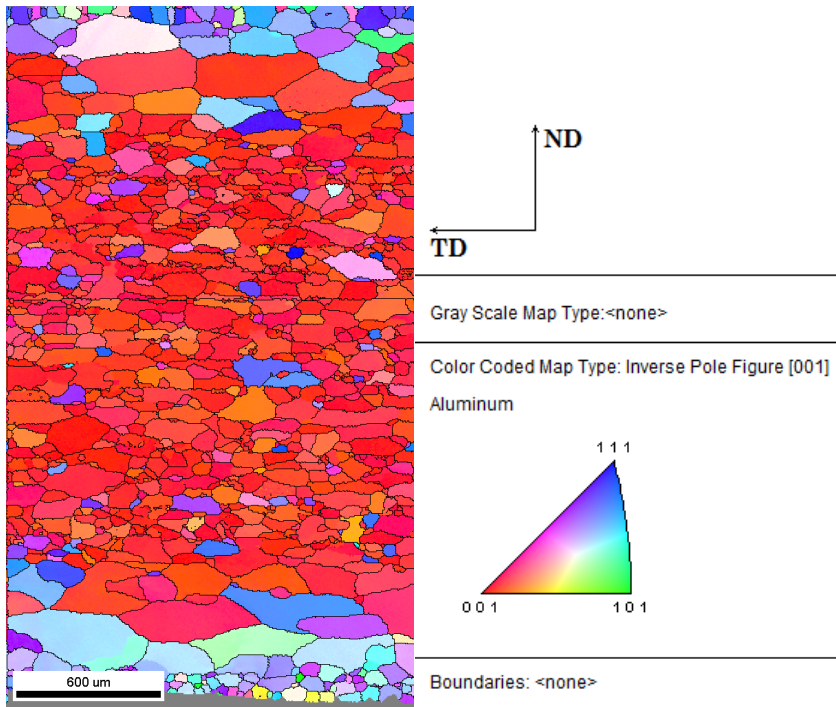


Figure 9: Electron backscatter diffraction (EBSD) scan showing the morphology, size and orientation of the grains through the thickness of the extruded AA6063 profile in the plane normal to the extrusion direction.

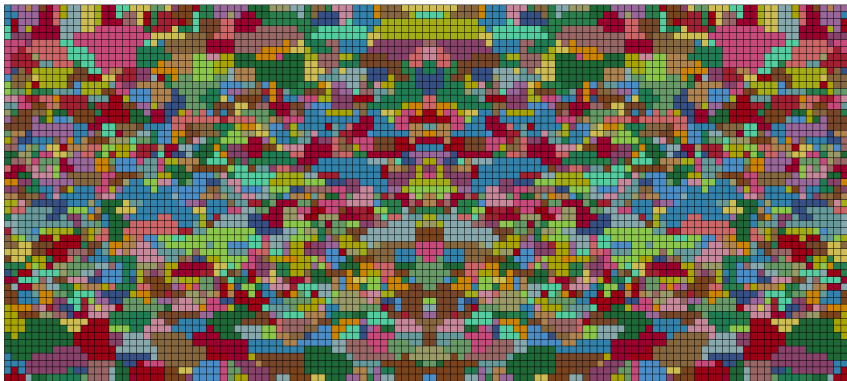


Figure 10: The EBSD scan with grain morphology mirrored around the left edge line of the scan (top), which was used as a basis for the CP-FEM model, and the CP-FEM mesh used in the calibration procedure of the hardening model (bottom).

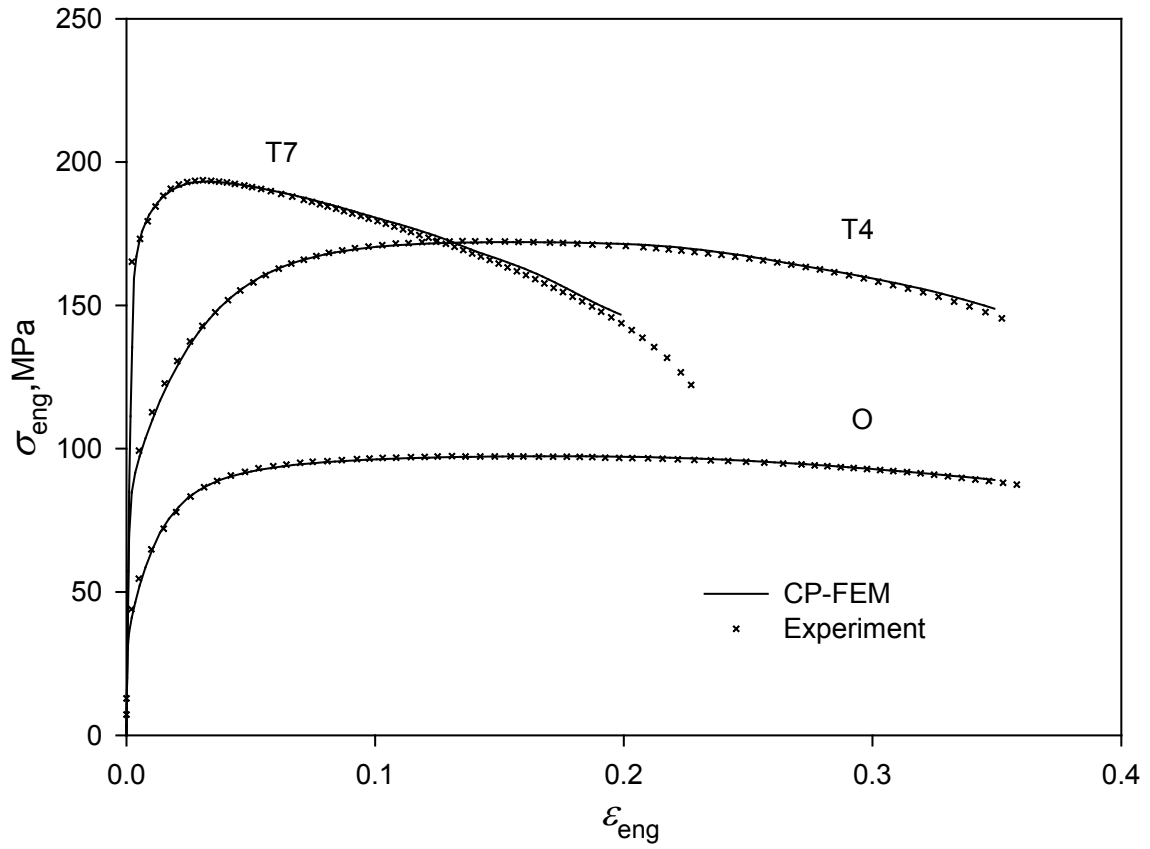


Figure 11: The results of the calibration of the crystal plasticity model in terms of engineering stress-strain curves from the experiments and the CP-FEM model used in the fitting procedure.

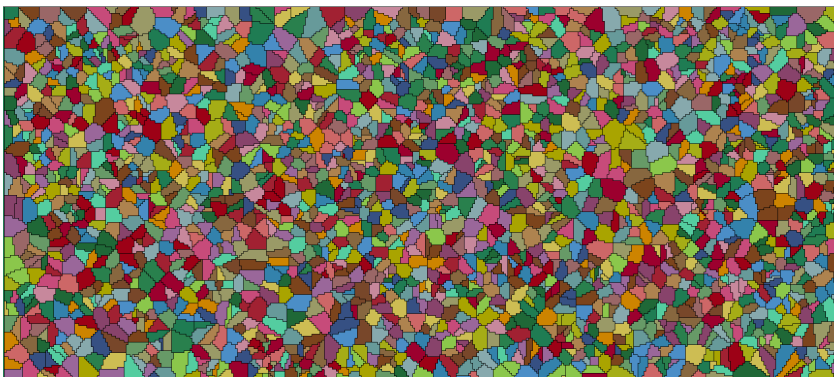
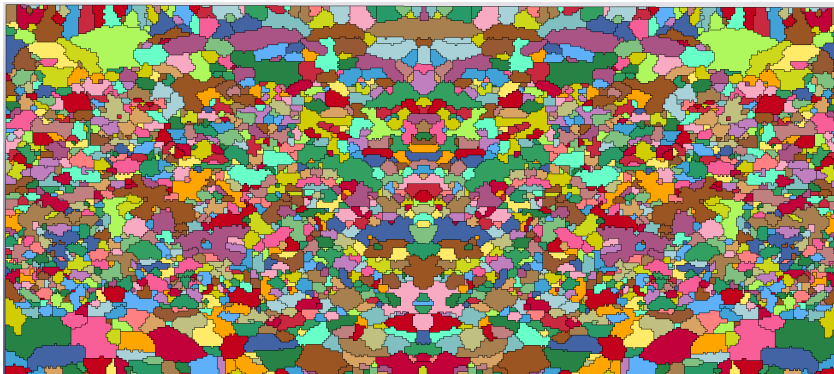


Figure 12: EBSD scan with grain morphology mirrored around the left edge line of the scan (top), CP-FEM mesh produced from the mirrored EBSD scan (middle), and CP-FEM mesh created by Voronoi tessellation (bottom).

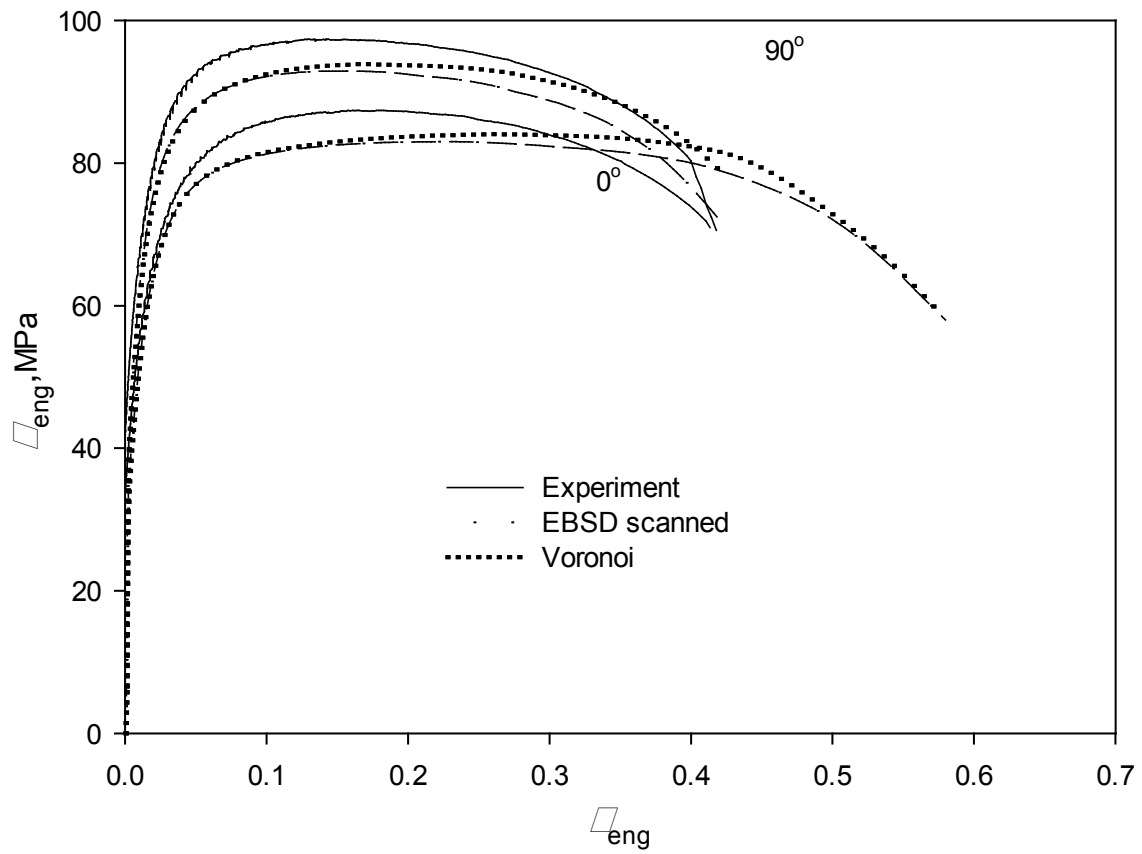


Figure 13: Engineering stress-strain curves in plane-strain tension from experiment and CP-FEM simulations with microstructure mapped from EBSD scan and Voronoi tessellation in two material directions for the O temper.

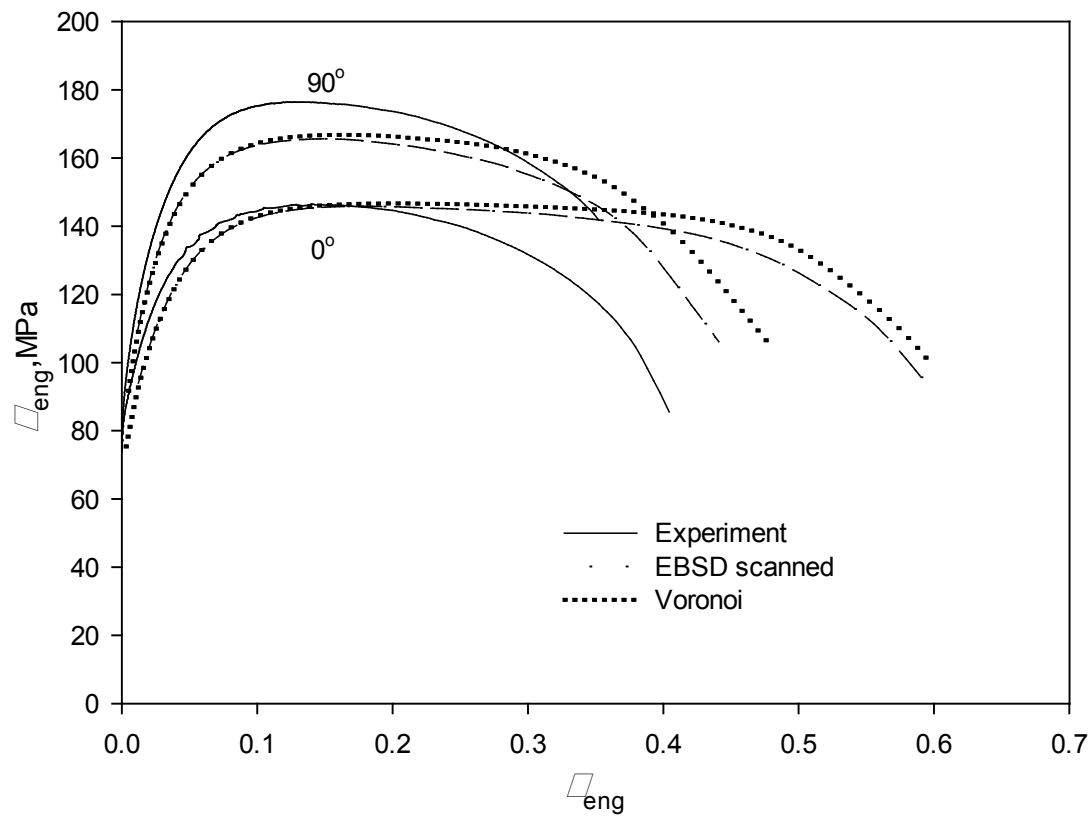


Figure 14: Engineering stress-strain curves in plane-strain tension from experiment and CP-FEM simulations with microstructure mapped from EBSD scan and Voronoi tessellation in two material directions for the T4 temper.

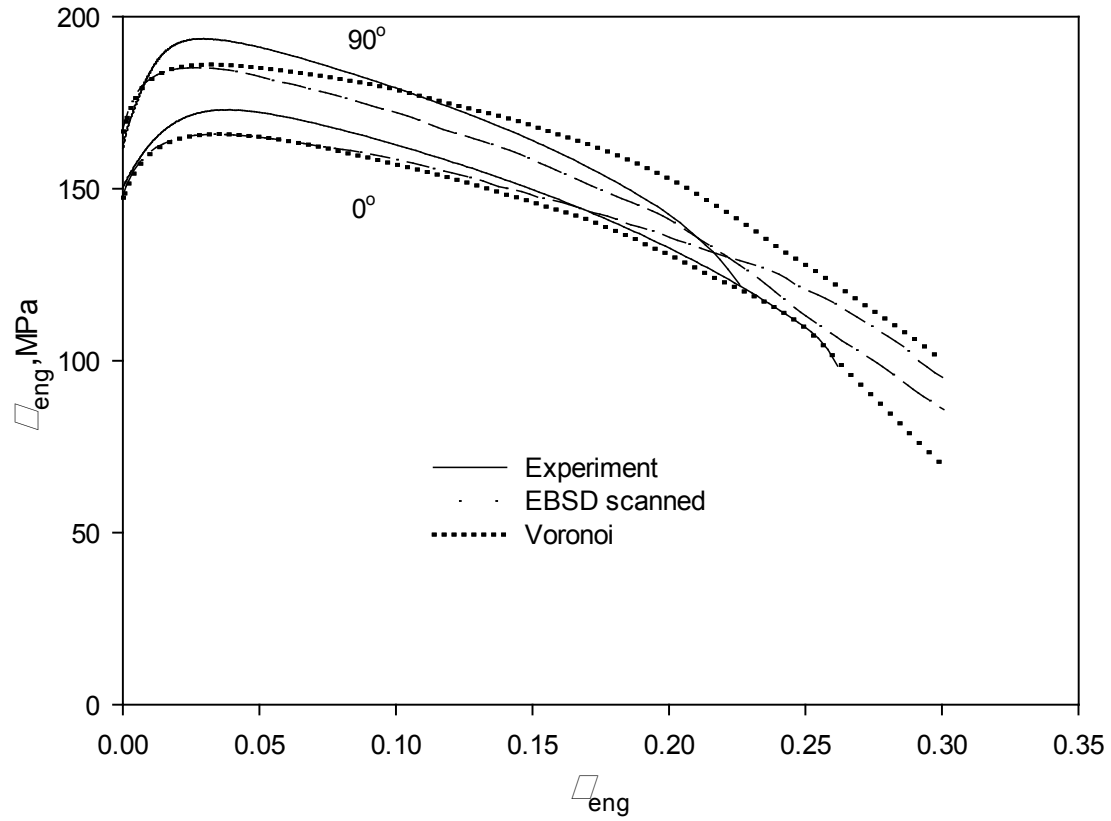


Figure 15: Engineering stress-strain curves in plane-strain tension from experiment and CP-FEM simulations with microstructure mapped from EBSD scan and Voronoi tessellation in two material directions for the T7 temper.



Figure 16: Three-dimensional FEM mesh of the plane-strain tension specimen.

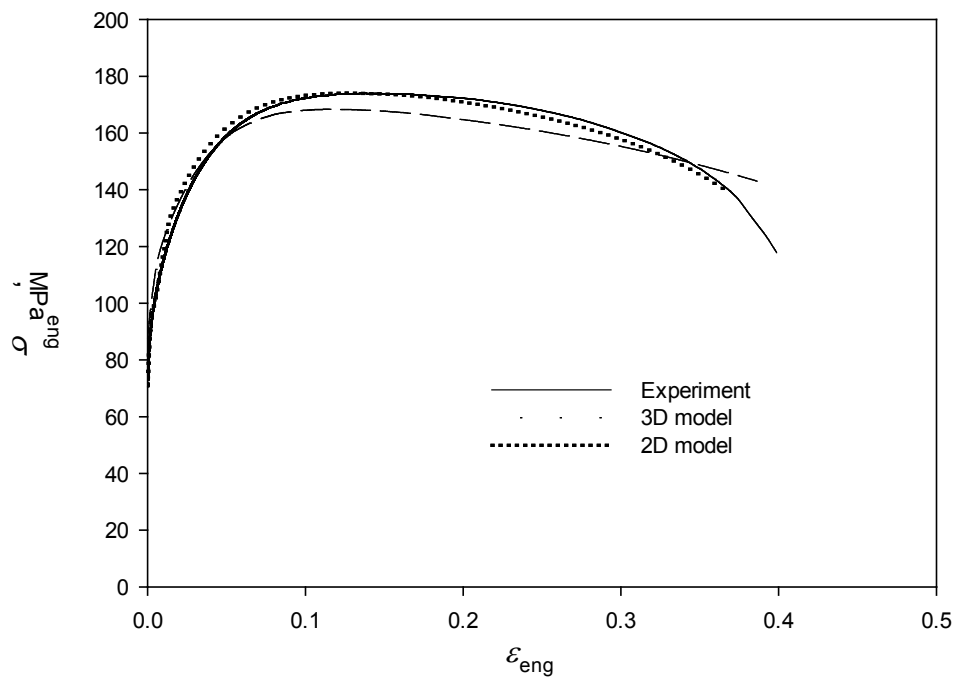


Figure 17: Engineering stress-strain curves from simulations with the two- and three-dimensional FEM models of the plane-strain tension specimen and the experiment for temper T4 in the 90° direction.

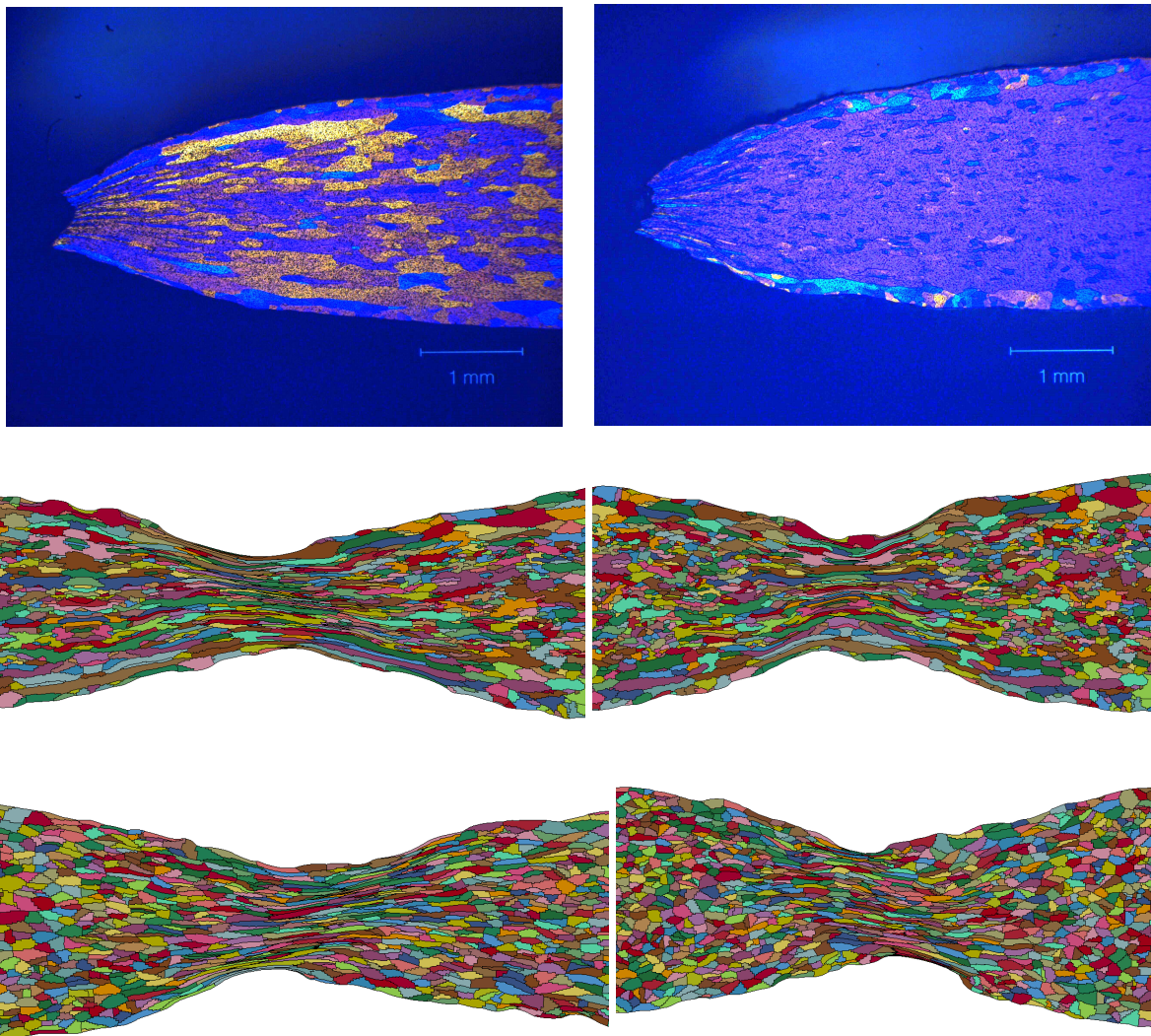


Figure 18: Optical photographs (top) and deformed meshes from the CP-FEM simulation of plane-strain tension with EBSD-mapped microstructure (middle) and microstructure based on Voronoi tessellation (bottom) for O temper in  $0^\circ$  orientation (left) and  $90^\circ$  orientation (right).

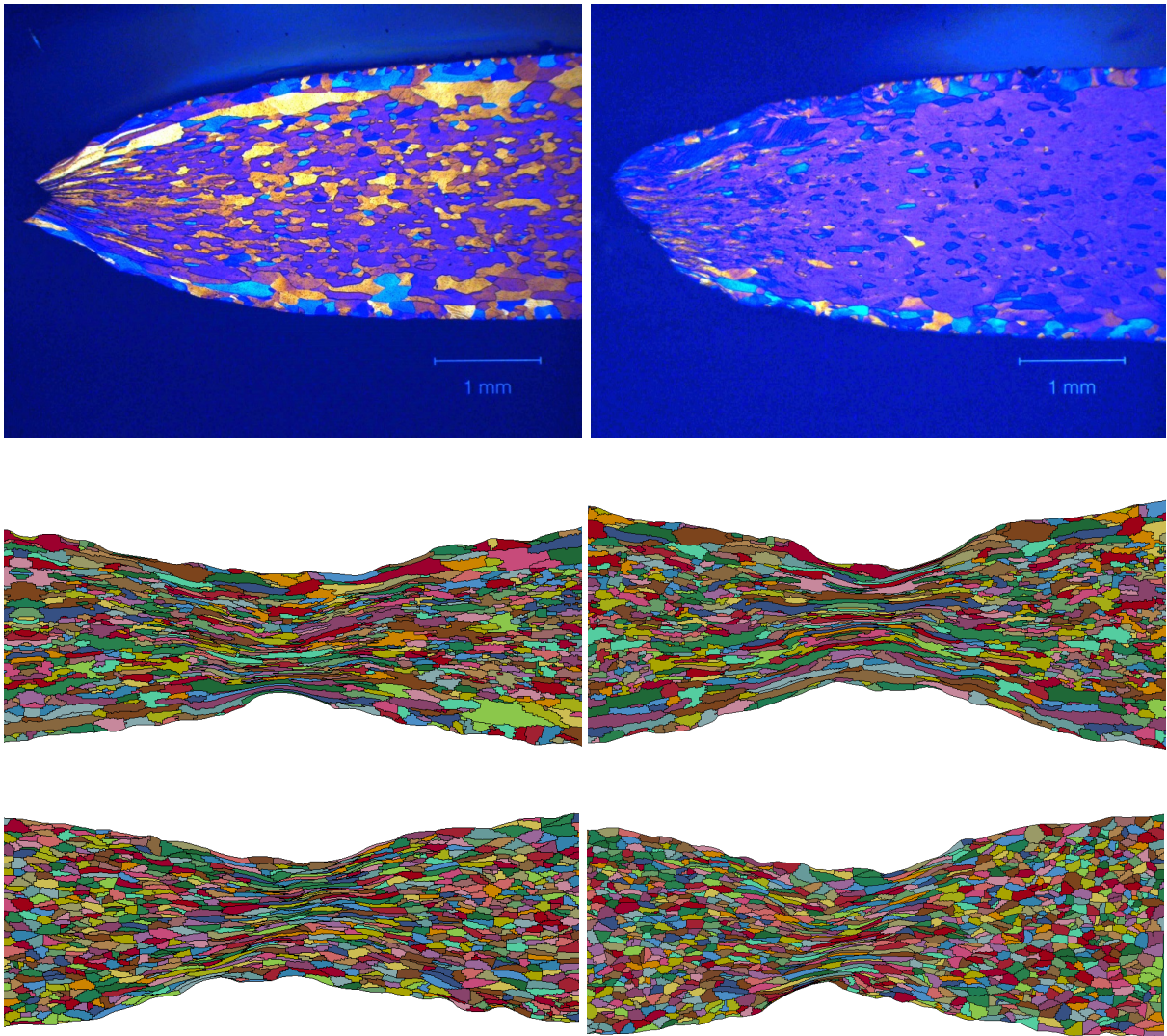


Figure 19: Optical photographs (top) and deformed meshes from the CP-FEM simulation of plane-strain tension with EBSD-mapped microstructure (middle) and microstructure based on Voronoi tessellation (bottom) for T4 temper in 0° orientation (left) and 90° orientation (right).

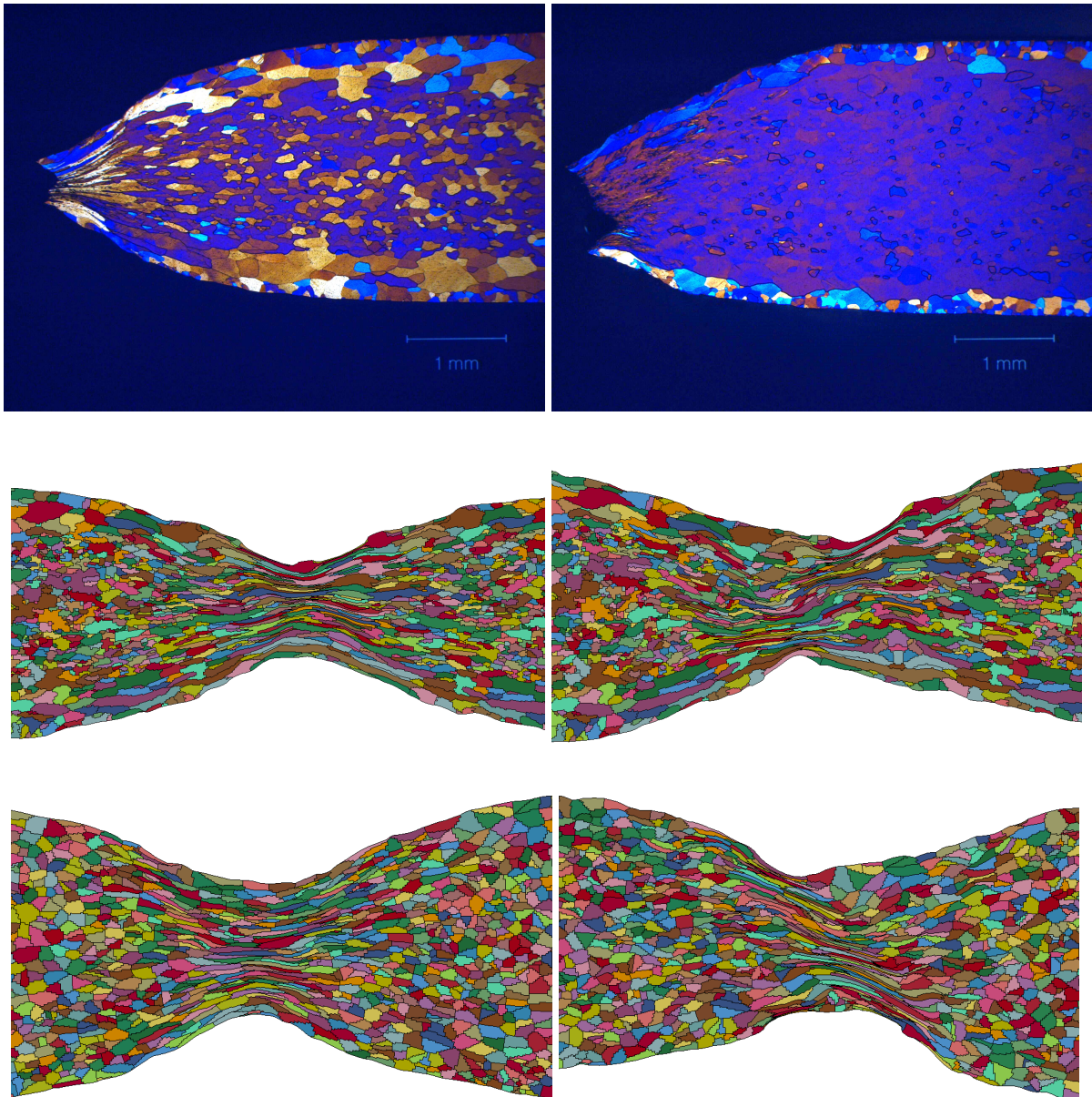


Figure 20: Optical photographs (top) and deformed meshes from the CP-FEM simulation of plane-strain tension with EBSD-mapped microstructure (middle) and microstructure based on Voronoi tessellation (bottom) for T7 temper in  $0^\circ$  orientation (left) and  $90^\circ$  orientation (right).

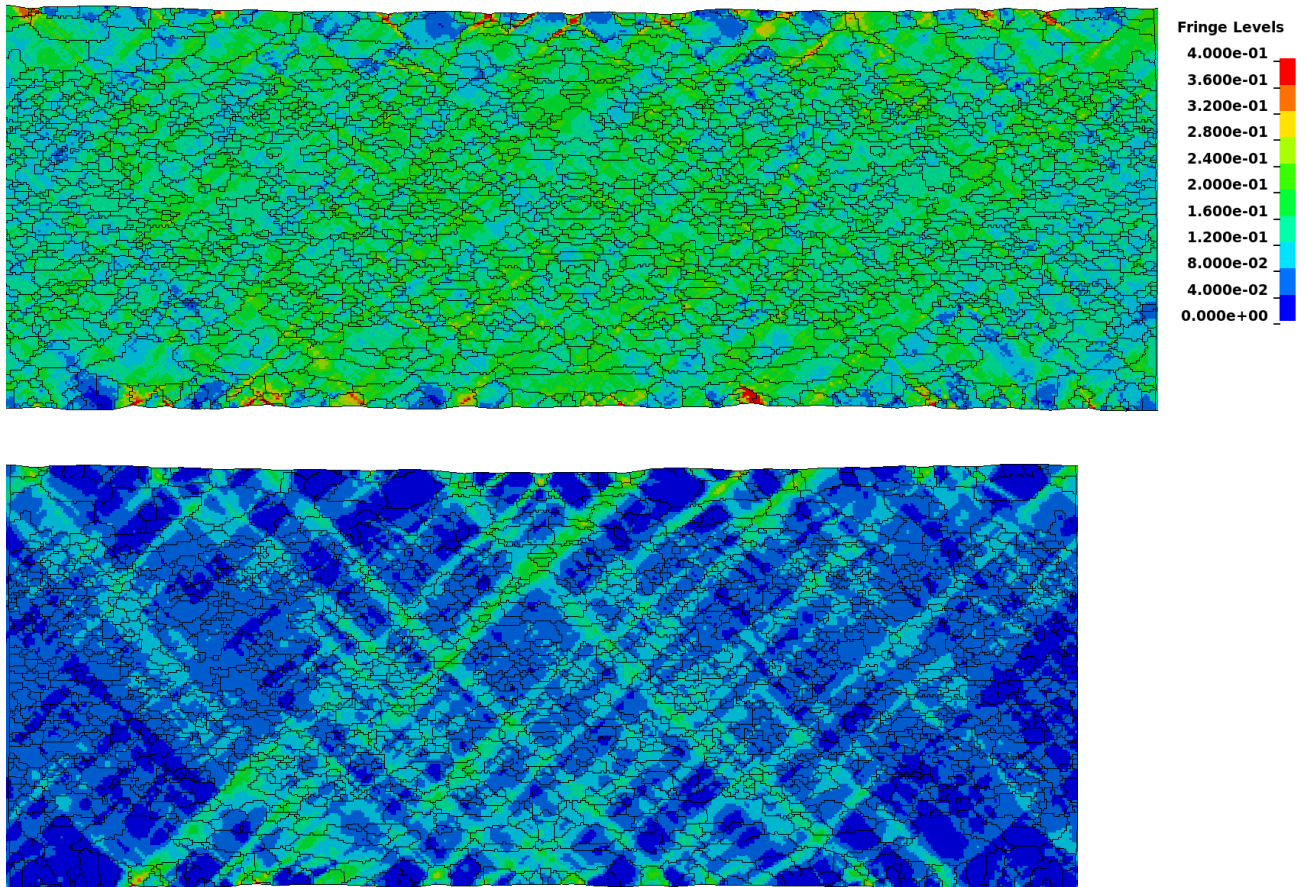


Figure 21: Contours of the von Mises equivalent strain from CP-FEM simulation of plane-strain tension with realistic microstructure for temper T4 in the  $0^\circ$  orientation at 13% global strain (top) and T7 in the  $0^\circ$  orientation at 6% global strain (bottom).

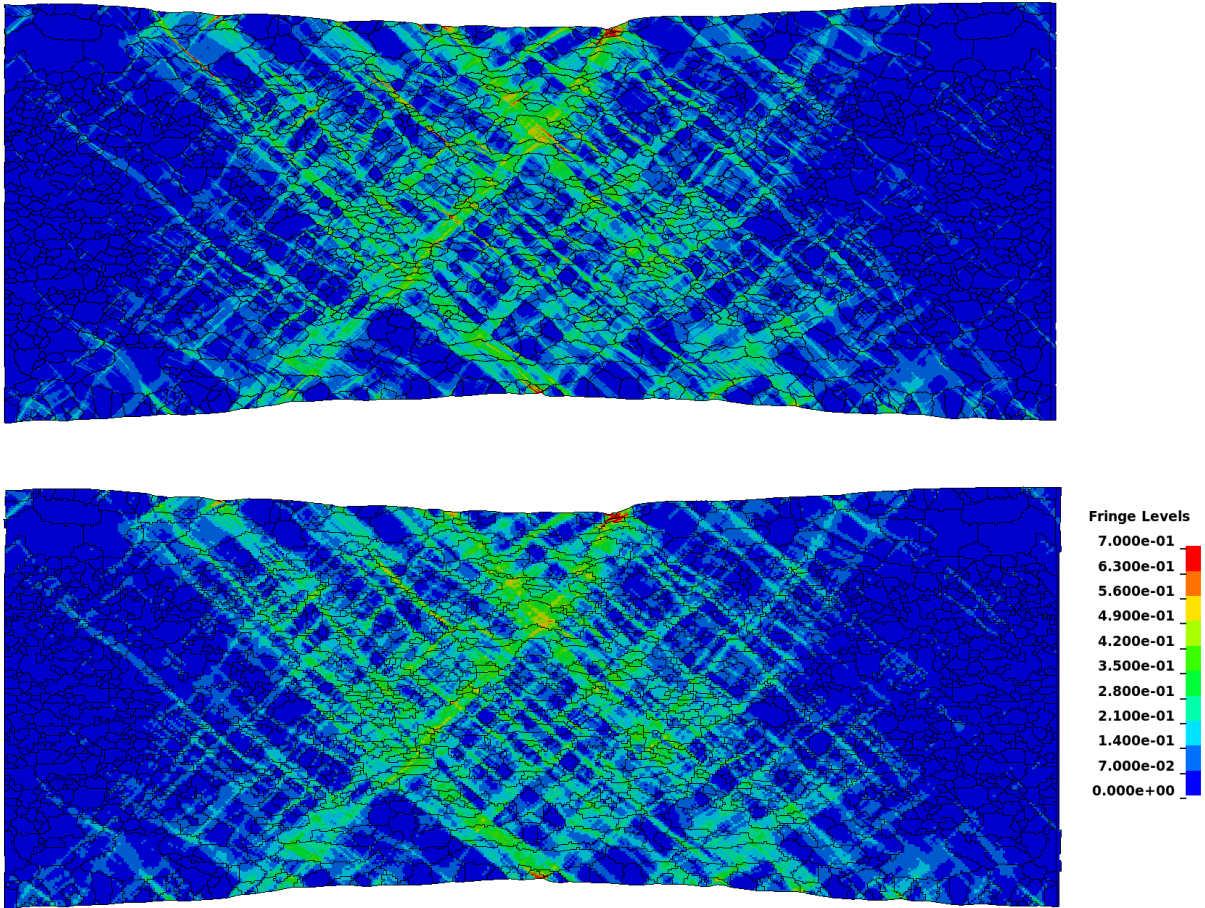


Figure 22: Contours of the von Mises equivalent strain for refined (top) and baseline (bottom) CP-FEM mesh for T7 temper in the 90° orientation.

## Tables

Table 1: Heat treatment of the alloys.

Temper	Stage 1	Stage 2	Stage 3	Stage 4	Stage 5
T4	540°C in salt bath for 15 min	Water quenching	One week at room temperature	—	—
T7	540°C in salt bath for 15 min	Water quenching	15 min at room temperature	185°C in oil bath for one week	Air cooling
O	540°C in salt bath for 15 min	Water quenching	15 min at room temperature	350°C in salt bath for twenty four hours	Air cooling

Table 2: Parameters of the crystal plasticity model taken from [67]

$c_{11}$ ,	$c_{12}$ ,	$c_{44}$ ,	$\dot{\gamma}_0$ ,	$m$	$q_{\alpha\beta}$	$\mu$ ,
MPa	MPa	MPa	$s^{-1}$			MPa
106430	60350	28210	0.010	200	1.4, if $\alpha \neq \beta$  1.0, if $\alpha = \beta$	24400

Table 3: Hardening parameters of the crystal plasticity model obtained by optimisation.

Temper	$\tau_0$ , MPa	$\tau_1$ , MPa	$\theta_1$ , MPa	$\tau_2$ , MPa	$\theta_2$ , MPa	$\tau_3$ , MPa	$\theta_3$ , MPa
T4	30.00	26.37	244.27	38.10	11.79	—	—
T7	60.00	8.30	193.61	12.01	1.77	—	—
O	12.00	12.97	350.10	5.87	35.88	75.82	5.62

Table 4: Parameters of the two-term Voce hardening rule used in the  $J_2$  flow theory.

Temper	Orientation	$\kappa_0$ , MPa	$Q_1$ , MPa	$\theta_1$ , MPa	$Q_2$ , MPa	$\theta_2$ , MPa
O	0°	25.0	55.44	3497.71	24.18	217.37
	90°	34.5	55.26	3346.54	37.25	302.47
T4	0°	63.0	72.14	1857.60	620.74	155.11
	90°	78.6	80.28	1984.57	787.50	86.62
T7	0°	122.8	30.99	2740.13	17.68	105.90
	90°	142.5	29.00	2856.67	28.79	42.89